

The dual role of starburst and active galactic nuclei in driving extreme molecular outflows

AVANI GOWARDHAN,¹ HENRIK SPOON,¹ DOMINIK A. RIECHERS,¹ EDUARDO GONZÁLEZ-ALFONSO,^{2,3} DUNCAN FARRAH,⁴
JACQUELINE FISCHER,⁵ JEREMY DARLING,⁶ CHIARA FERGULIO,⁷ JOSE AFONSO,^{8,9} LUCA BIZZOCCHI¹⁰

¹*Department of Astronomy, Cornell University, Ithaca, NY 14853, USA*

²*Universidad de Alcalá, Departamento de Física y Matemáticas, Campus Universitario, E-28871 Alcalá de Henares, Madrid, Spain*

³*Harvard-Smithsonian Center for Astrophysics, 60 Garden Street, Cambridge, MA 02138, USA*

⁴*Department of Physics, Virginia Tech, Blacksburg, VA 24061, USA*

⁵*Naval Research Laboratory, Remote Sensing Division, 4555 Overlook Avenue SW, Washington DC 20375, USA*

⁶*Center for Astrophysics and Space Astronomy, Department of Astrophysical and Planetary Sciences, University of Colorado, 389 UCB, Boulder, CO 80309-0389, USA*

⁷*INAF Osservatorio Astronomico di Trieste, via G.B. Tiepolo 11, 34143, Trieste, Italy*

⁸*Instituto de Astrofísica e Ciências do Espaço, Universidade de Lisboa, OAL, Tapada da Ajuda, PT1349-018 Lisboa, Portugal*

⁹*Departamento de Física, Faculdade de Ciências, Universidade de Lisboa, Edifício C8, Campo Grande, PT1749-016 Lisbon, Portugal*

¹⁰*Center for Astrochemical Studies, Max-Planck-Institut für extraterrestrische Physik, Gießenbachstraße 1, 85748 Garching, Germany*

ABSTRACT

We report molecular gas observations of IRAS 20100–4156 and IRAS 03158+4227, two local ultra-luminous infrared galaxies (ULIRGs) hosting some of the fastest and most massive molecular outflows known. Using ALMA and PdBI observations, we spatially resolve the CO(1 – 0) emission from the outflowing molecular gas in both and find maximum outflow velocities of $v_{\max} \sim 1600$ and ~ 1700 km s^{−1} for IRAS 20100–4156 and IRAS 03158+4227, respectively. We find total gas mass outflow rates of $\dot{M}_{\text{OF}} \sim 670$ and $\sim 350 M_{\odot} \text{ yr}^{-1}$, respectively, corresponding to molecular gas depletion timescales $\tau_{\text{OF}}^{\text{dep}} \sim 11$ and ~ 16 Myr. This is nearly 3 times shorter than the depletion timescales implied by star formation, $\tau_{\text{SFR}}^{\text{dep}} \sim 33$ and ~ 46 Myr, respectively. To determine the outflow driving mechanism, we compare the starburst (L_{\star}) and AGN (L_{AGN}) luminosities to the outflowing energy and momentum fluxes, using mid-infrared spectral decomposition to discern L_{AGN} . Comparison to other molecular outflows in ULIRGs reveals that outflow properties correlate similarly with L_{\star} and L_{IR} as with L_{AGN} , indicating that AGN luminosity alone may not be a good tracer of feedback strength and that a combination of AGN and starburst activity may be driving the most powerful molecular outflows. We also detect the OH 1.667 GHz maser line from both sources and demonstrate its utility in detecting molecular outflows.

1. INTRODUCTION

Numerous observations suggest a close evolutionary relationship between supermassive black hole (SMBH) growth and stellar assembly in massive galaxies. These include the strong correlation between SMBH mass (M_{BH}) and stellar bulge properties i.e. its mass (M_{bulge}) and velocity dispersion (σ ; Magorrian et al. 1998; Ferrarese & Merritt 2000; Gebhardt et al. 2000; McConnell & Ma 2013). Furthermore, the observed galaxy luminosity function declines more steeply at high luminosities $L > L^*$ (Baugh et al. 1998) than predicted based on Λ CDM hierarchical structure formation models, sug-

gesting that star formation is suppressed in massive galaxies ($M^* > 10^{11} M_{\odot}$ at $z \sim 0$). Galaxy evolution models often invoke some form of feedback from active galactic nuclei (AGN) to quench star formation and reconcile luminosity function models with these observations (Benson et al. 2003; Bower et al. 2006; Somerville et al. 2008). Two main forms of feedback have been incorporated into models - radio (‘maintenance mode’) and radiative (‘quasar mode’) feedback. Radio mode feedback is associated with lower accretion rates (e.g. Ishibashi et al. 2014), takes place in the form of highly-collimated and relativistic radio jets, and is typically seen in early-type galaxies (i.e. in giant ellipticals at low- z). In contrast, radiative feedback results when the SMBH approaches the Eddington accretion rate, producing energetic nuclear winds that collide with the interstellar medium (ISM), generating a blast wave which

drives out the dust and cold gas in the form of massive outflows, thus quenching star formation and growth of the stellar bulge (Lapi et al. 2005; King 2010; Zubovas & King 2012). In the classic galaxy evolution picture, this is the crucial step in the evolution from dusty, obscured AGN host galaxies to unobscured and optically luminous quasars, and therefore important at high- z . Local ultraluminous infrared galaxies (ULIRGs) hosting powerful AGN and/or starburst activity are ideal targets in which to study feedback physics and its role in galaxy evolution, being local analogs of the dusty star-forming galaxy (DSFG) population at high- z (see Casey et al. 2014, for a review).

While ULIRGs often show prominent ionized and neutral gas outflows (e.g. Rupke et al. 2005; Spoon & Holt 2009), observations of outflowing molecular gas - the fuel for star formation - are necessary to definitively identify quenching of star formation. Molecular outflows have been detected in *Herschel* observations of ULIRGs using far-IR transitions (OH 119 μm and OH 79 μm), which trace the outflows close to the central nucleus (~ 300 pc, flow times $\tau \sim \text{few} \times 10^5$ yrs; Fischer et al. 2010; Sturm et al. 2011; González-Alfonso et al. 2017) and show a characteristic P-Cygni profile, providing unambiguous evidence of outflowing gas. Further observations of local ULIRGs demonstrate that energetically dominant AGN hosts have higher maximum gas outflow velocities (up to $\sim 1400 - 2000$ km s $^{-1}$; Fischer et al. 2010; Sturm et al. 2011; Spoon et al. 2013; Veilleux et al. 2013) as compared to those dominated by starburst activity. CO(1–0) observations of such ULIRGs trace the outflow on larger spatial (up to ~ 10 kpc) and longer time scales (flow times $\tau \gtrsim 10^6$ yrs) than the far-IR OH transitions, and demonstrate that the molecular gas can be depleted on short timescales ~ 10 Myr (e.g. Feruglio et al. 2010; Cicone et al. 2014). Finally, both OH and CO(1–0) observations for a sample of nearby galaxies hosting outflows show increasing mass outflow rates and higher outflow velocities with increasing AGN luminosities, interpreted by the authors as more powerful molecular outflows being mostly powered by AGN (e.g. Fischer et al. 2010; Sturm et al. 2011; Spoon et al. 2013; Veilleux et al. 2013; Cicone et al. 2014; Stone et al. 2016). However, there are many open questions in this picture of galaxy evolution. While outflows in massive galaxies are ubiquitous, their impact on star formation is still debated, with some studies finding that outflows decrease the star formation (e.g. Farrah et al. 2012; Alatalo et al. 2015), and others finding no difference in star formation (e.g. Violino et al. 2016; Pitchford et al. 2016; Bal-maverde et al. 2016). The driving mechanism of outflows is also still an open question. Nuclear starburst

and AGN activity are often observed concurrently in ULIRGs (e.g. Genzel et al. 1998; Farrah et al. 2002, 2003; Veilleux et al. 2009; Efstathiou et al. 2014; Xu et al. 2015; Rosenberg et al. 2015). This makes it difficult to identify the respective roles of AGN and starburst activity in ULIRGs, especially given the high nuclear dust obscuration in most ULIRGs. It is also debated how nuclear starbursts relate to AGN activity: numerical simulations variously show that starbursts can both precede AGN activity and SMBH growth (e.g. Hopkins 2012), or can be triggered by AGN feedback (e.g. Silk & Nusser 2010; Ishibashi et al. 2013). It has also been proposed that both star formation and SMBH growth are independent and self-regulatory (Cen 2012) and that the observed bulge-BH correlations are produced by hierarchical structure formation (e.g. Jahnke & Macciò 2011) rather than feedback processes. Observations of outflowing molecular gas provide critical insight into these open questions. Molecular gas not only traces the fuel for star formation but can also make up the bulk of the outflowing gas mass. Spatially resolved molecular gas observations can be used to determine the outflow energetics, distinguish between outflow models, and determine the driving mechanism.

Here we present observations of two local ULIRGs hosting the most extreme molecular outflows in the local Universe - IRAS 20100–4156 and IRAS 03158+4227, both at $z \sim 0.13$. The sources have been selected from the *Herschel* ULIRG Survey (HERUS), a complete, flux-limited ($S_{60\mu\text{m}} > 1.9$ Jy) far-IR spectroscopic sample of the local ULIRG population (Farrah et al. 2013; Pearson et al. 2016a). While molecular outflows are ubiquitous in this and other samples of local ULIRGs (Spoon et al. 2013; Veilleux et al. 2013), the two selected sources display the deepest absorption profiles in far-IR OH lines and/or the highest maximum outflow velocities in their OH 119 μm spectra (Spoon et al. 2013; González-Alfonso et al. 2017), even more so than the archetypal outflow source, Mrk 231 (Fischer et al. 2010; Spoon et al. 2013; González-Alfonso et al. 2017). Such high-velocity outflows are expected to be much more common at high- z (e.g. Maiolino et al. 2012), making it crucial to understand their origin and impact on the host galaxy. We present spatially resolved observations of the outflowing molecular gas in both these sources - traced using CO(1–0) - to determine the outflow properties (geometry, outflow rate, and energetics), while simultaneously using multi-wavelength spectroscopy and extensive photometric coverage (from mid-IR to X-ray) to identify the relative AGN and starburst contributions, and relate them to the outflow properties. Finally, we also present observations of the OH 1.667 GHz maser line (hereafter

OHM) in our targets and demonstrate its utility for future molecular gas studies.

The paper is organized as follows: in § 2 and § 3, we present the observations and results. In § 4, we discuss the outflow properties, spectral energy distribution (SED) fitting, and mid-IR spectral decomposition. In § 5 and § 6, we discuss our results and conclusions. We use a Λ CDM cosmology, with $H_0 = 71 \text{ km s}^{-1} \text{ Mpc}^{-1}$, $\Omega_M = 0.27$, and $\Omega_\Lambda = 0.73$ (Spergel et al. 2007).

2. OBSERVATIONS

In this section, we discuss the details of molecular gas observations (summarized in Table 1) as well as existing observations in the literature in § 2.3.

2.1. CO observations

2.1.1. CO(1–0) in IRAS 20100–4156

We observed the CO(1–0) line in IRAS 20100–4156 using the Atacama Large Millimeter Array (ALMA), over 5 epochs in June 2014 with 37 antennas (PI: Spoon). The absolute flux scale was calibrated using Neptune and Uranus, while J2056–4714 was used as a bandpass and phase calibrator. The receivers were tuned to a central frequency of 102.055 GHz, with a bandwidth of 1.875 GHz in each of 4 spectral windows, corresponding to 3840 frequency channels with a channel width of 0.49 MHz ($\sim 1.4 \text{ km s}^{-1}$).

CASA v4.2 was used for the ALMA pipeline calibration, and the resulting measurement set was used for all further analysis. Continuum subtraction was performed using the task UVCONTSUB, using line-free channels and spectral windows (a total bandwidth of 2902 MHz), using a 1st order polynomial baseline for the continuum. This calibrated and continuum-subtracted visibility dataset was used for the task UVMODELFIT. Prior to using UVMODELFIT, the task STATWT was used to calculate the weights for the visibilities based on line-free channels only. The reduced measurement set was imaged and cleaned using the CASA task CLEAN, using natural weighing and a pixel size of $0''.3 \times 0''.3$, after binning over 71 spectral channels (corresponding to $\sim 100 \text{ km s}^{-1}$). The resulting cleaned image has an rms noise of $0.1 \text{ mJy beam}^{-1}$ over each channel with width 34 MHz, (corresponding to $\sim 100.2 \text{ km s}^{-1}$ at 102.055 GHz), and a resulting synthesized beam size of $1''.5 \times 1''.2$ (PA = 75°). As the emission is resolved both in velocity as well as spatially, the clean mask for the emission region was selected after visual inspection for each channel.

2.1.2. CO(3–2) in IRAS 20100–4156

We observed CO(3–2) emission in IRAS 20100–4156, redshifted to $\nu_{\text{obs}} = 306.082 \text{ GHz}$, using the single

dish sub-mm telescope Atacama Pathfinder Experimental telescope (APEX) over 8 epochs from August - October 2012 (PI: Farrah), for a total on-source time of 3.7 hours. The weather ranged from good (with the atmospheric precipitable water vapor (pwv) $\sim 0.5 \text{ mm}$) to acceptable (pwv $\sim 4 \text{ mm}$) during the observations. The APEX-2 heterodyne receiver was used as a front-end with the eXtended bandwidth Fast Fourier Transform Spectrometer (XFFTS) as the backend, with wobbler-switching at a frequency of 0.5 Hz and an asymmetrical azimuthal throw of $50''$. Saturn and RZ-Sgr were used for pointing. The total bandwidth was 2.5 GHz, centered at 306.0119 GHz, with a frequency resolution of 76.3 kHz, which corresponds to a velocity resolution of 0.074 km s^{-1} . The half-power beam width at this frequency is $\sim 21''$, so the emission was unresolved. Data reduction was carried out using GILDAS CLASS (Continuum and Line Analysis Single-dish Software), and the spectrum was binned to a velocity resolution of $\sim 53 \text{ km s}^{-1}$. The antenna temperatures (T_A) were converted to flux densities assuming an aperture efficiency of $\eta_a = 0.6$, which implies a K to Jy conversion factor $24.4/\eta_a = 41 \text{ Jy K}^{-1}$ ¹. The final spectrum has an rms noise of 0.6 mJy over a line-free bandwidth of $\sim 3300 \text{ km s}^{-1}$.

2.1.3. CO(1–0) in IRAS 03158+4227

We observed CO(1–0) emission toward IRAS 03158+4227 with the Plateau de Bure Interferometer (PdBI) in the most compact 5 antenna configuration (5D), during July-August 2013 (PI: Spoon). The weather was average during these observations (pwv $\sim 10 \text{ mm}$ on average). The quasars 3C84 and B0234+285 were used as phase and amplitude calibrators respectively, and the quasars 3C84 and 3C345 were used as RF bandpass calibrators. The star MWC349 and the quasar 3C454.3 were used as absolute flux calibrators. The WideX correlator with a bandwidth of 3.6 GHz was tuned to 101.604 GHz, and the observations were carried out in dual polarization mode, with a spectral resolution of 1.95 MHz (corresponding to $\sim 5.8 \text{ km s}^{-1}$). The total on-source time, after flagging of bad visibilities was 19.5 hours (6 antenna equivalent time, summing together 18 observations). Given the large bandwidth of the observations, we also covered CN($N = 1 - 0$, $J = 3/2 - 1/2$), redshifted from $\nu_{\text{rest}} \sim 113.490 \text{ GHz}$ to $\nu_{\text{obs}} = 100.04612 \text{ GHz}$.

All observations were calibrated using the IRAM PdBI data reduction pipeline in CLIC (Continuum and Line Interferometer Calibration), with subsequent additional

¹ <http://www.apex-telescope.org/telescope/efficiency>

flagging by hand. The absolute flux scale was calibrated to better than 20%. Continuum subtraction was performed for the reduced visibility cube using the task UV_SUBTRACT, excluding the line channels (a total of 2.64 GHz of line-free bandwidth). The resulting continuum-subtracted visibility data was imaged using UV_MAP, with natural weighting and a pixel size of $0''.5 \times 0''.5$, and cleaned using the task CLEAN with the Hogbom algorithm at a binned spectral resolution of 20 MHz ($\sim 60 \text{ km s}^{-1}$ at a frequency of 101.604 GHz). The resulting cleaned image has an rms noise of $0.26 \text{ mJy beam}^{-1}$ over each 20 MHz channel, and a beam size of $4''.8 \times 3''.9$ (PA = 166°). Primary beam correction was applied using the task PRIMARY.

2.2. OHM observations

We observed the OH 1.667 GHz maser line for both IRAS 20100–4156 and IRAS 03158+4227, using the NSF’s Karl G. Jansky Very Large Array (VLA) in August 2015, as part of a Director’s Discretionary Time (DDT) proposal (PI: Spoon). Observations were made using the L band receivers in the most extended configuration (A array), using 27 antennas. We used a bandwidth of 1 GHz over 8 spectral windows with a bandwidth of 128 MHz for each sub-band, with spectral resolutions of 111 kHz and 142 kHz in the spectral windows covering the lines for IRAS 20100–4156 and IRAS 03158+4227, respectively. The receivers were tuned to central frequencies of 1.411 GHz and 1.407 GHz, respectively.

IRAS 20100–4156 was observed for a total on-source time of 90 minutes. 3C48 and J1937–3958 were used for absolute flux and phase/bandpass calibration respectively. IRAS 03158+4227 was observed for a total on-source time of 20 minutes. 3C147 and J0319+4130 were used for absolute flux and phase/bandpass calibration, respectively.

The VLA reduction pipeline in CASA v4.3.1 was used to flag and calibrate the observations. Continuum subtraction was performed based on the line-free channels (total line-free bandwidth of ~ 0.7 GHz for both using the task UVCONTSUB, using a 1st order fit for the continuum. For IRAS 20100–4156, the reduced measurement set was cleaned using the CASA task CLEAN, using natural weighting and a pixel size of $0''.5 \times 0''.5$. The resulting cleaned image has an rms noise of $0.8 \text{ mJy beam}^{-1}$ over each channel of 142 kHz (corresponding to $\sim 30.2 \text{ km s}^{-1}$ at 1.411 GHz), and a synthesized beam size of $4''.9 \times 1''.0$ (PA: -175°).

For IRAS 03158+4227, the same pipeline was used for flagging and calibration. Continuum subtraction was performed using a linear 1st order fit to line-free chan-

nels. The CASA task CLEAN was used with natural weighting and a pixel size of $0''.5 \times 0''.5$, after binning over 5 velocity channels (each corresponding to 111 kHz). The resulting cleaned image has an rms noise of $1.0 \text{ mJy beam}^{-1}$ over each 565 kHz channel (corresponding to a velocity resolution of 120 km s^{-1} at 1.407 GHz) and a synthesized beam size of $1''.6 \times 1''.3$ (PA: -45.58°).

2.3. Archival Data

Extensive photometric and spectroscopic coverage exists for both our target sources. The photometric coverage includes X-ray observations from XMM Newton, far-UV and near-UV observations from GALEX, and both mid- and far-IR observations (spectroscopy as well as photometry) using *Herschel* PACS/SPIRE and the *Spitzer* InfraRed Spectrograph (IRS; Houck et al. 2004). Details of the photometry used and their references are listed in Table 2. Optical imaging was obtained using the *Hubble Space Telescope* Wide Field and Planetary Camera 2 (HST/WFPC2) instrument (F814W band) for IRAS 20100–4156 (as part of the proposal IDs 6346, 7896, Cui et al. 2001; Bushouse et al. 2002), and the Sloan Digital Sky Survey (SDSS) for IRAS 03158+4227; (SDSS Collaboration et al. 2016). Astrometric corrections were determined for the F814W HST image using nearby stellar positions from the General Star Catalog 2, leaving residual uncertainties of $0''.2$. *Herschel* PACS observations of the far-IR fine-structure lines and OH 119 μm and 79 μm profiles were presented by Farrah et al. (2013) and Spoon et al. (2013), and modeling of these far-IR OH lines (as well as the OH 84 μm and OH 65 μm doublets) was presented in González-Alfonso et al. (2017).

We compare the outflow properties of IRAS 20100–4156 and IRAS 03158+4227 against molecular outflows in other local ULIRGs with published OH 119 μm and CO observations (Cicone et al. 2014; García-Burillo et al. 2015; Veilleux et al. 2017) in order to place our results in the larger context of molecular outflows using the most uniform sample possible based on outflow and galaxy properties. We use *Spitzer* mid-IR spectra for all the sources, available from the Combined Atlas of Sources with *Spitzer* IRS Spectra (CASSIS; Lebouteiller et al. 2011, 2015). The high sensitivity and spectral resolution of CO(1–0) observations mean that the CO-based redshifts are more accurate than previously accessible, and we use those for the rest of the paper.

3. RESULTS

3.1. IRAS 20100–4156

3.1.1. CO(1–0) emission

IRAS 20100–4156 is a two-component interacting system and we here refer to the two principal components

Table 1. Details of molecular gas observations of IRAS 20100–4156 and IRAS 03158+4227.

Source	Position	z_{CO}	Telescope	Transition	Beam size	T_{on} (hours)
IRAS 20100–4156	$20^{\text{h}}13^{\text{m}}29.5^{\text{s}} - 41^{\text{d}}47^{\text{m}}35^{\text{s}}$	0.12975	ALMA	CO(1–0)	$1''.5 \times 1''.2$	4.1
			VLA	OH($^2\Pi_{3/2}, J = 3/2, F = 2^e - 2^f$)	$4''.9 \times 1''.0$	1.5
			APEX	CO(3–2)	$21''$	3.7
IRAS 03158+4227	$03^{\text{h}}19^{\text{m}}12.4^{\text{s}} + 42^{\text{d}}38^{\text{m}}28^{\text{s}}$	0.13459	PdBI	CO(1–0)	$4''.8 \times 3''.9$	19.5
			PdBI	CN ($N = 1 - 0, J = 3/2 - 1/2$) ^a	$4''.8 \times 3''.9$	19.5
			VLA	OH($^2\Pi_{3/2}, J = 3/2, F = 2^e - 2^f$)	$1''.6 \times 1''.3$	0.3

^aWe observed only one component of the CN doublet.

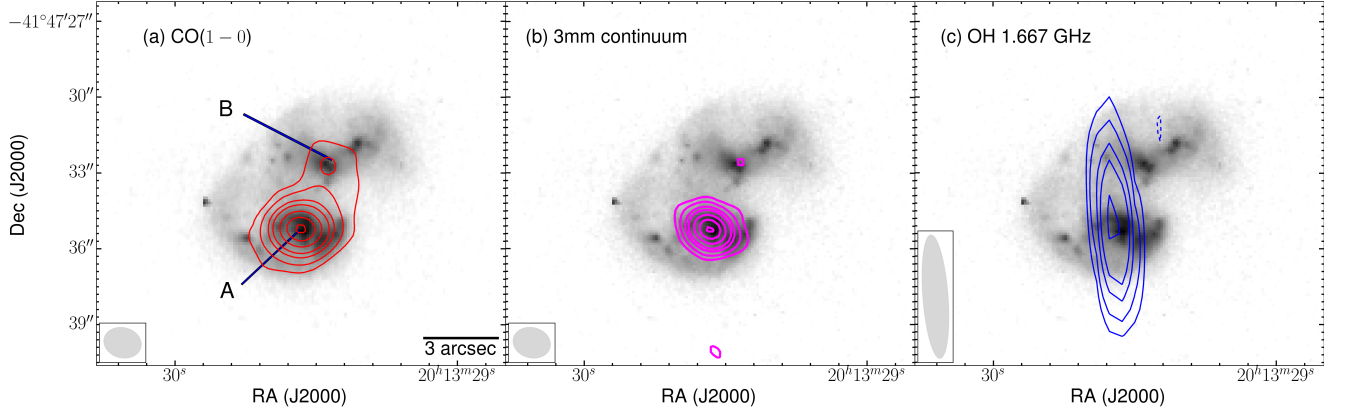


Figure 1. (a) Moment-0 map of CO(1–0) emission from IRAS 20100–4156, created by integrating over velocity range $(-1169, 1650)$ km s^{-1} , overlaid on a HST/WFPC2 F814W image (b) 3mm continuum emission (c) Moment-0 map of the OHM emission, created by integrating over the velocity range $(-927, 527)$ km s^{-1} , the peak of which is spatially offset from the peak of the dust and CO(1–0) emission (see § 3.1.4). Each panel shows contours marked at $\pm 3, 7, 15, 23, 40, 60, 80\sigma$ significance levels. The peaks of the two components of the merger (marked A and B) show a projected separation of 5.6 kpc. We detect the molecular gas outflow from component A. Synthesized beam sizes are $1''.5 \times 1''.2$ for (a) and (b), and $4''.9 \times 1''.0$ for (c), and are shown at the bottom left of each panel.

as A and B, respectively (Fig. 1). The two components have a projected separation of $\sim 2''.5$, corresponding to 5.6 kpc ($1'' \sim 2.287$ kpc at $z = 0.12975$). We detect and spatially resolve the CO(1–0) line emission between both components in the continuum-subtracted spectral line cube. The underlying continuum flux is $f_{\lambda} = 1.56 \pm 0.03$ mJy at $\lambda_{\text{obs}} = 2.96$ mm, using the line-free channels (Fig. 1). The dust emission predominantly emerges from component A, though we tentatively detect continuum emission at $\sim 3\sigma$ significance from component B, with a flux of $f_{\lambda} = 93 \pm 36$ μJy . We fit the line centroids in spectra extracted from the peak pixels of A and B with 1-D Gaussian line profiles (Fig. 2), and find velocity widths of $\Delta v_{\text{FWHM}}^{\text{A}} \sim 371.4 \pm 4.2$ km s^{-1} and $\Delta v_{\text{FWHM}}^{\text{B}} \sim 111.8 \pm 8.2$ km s^{-1} , respectively, with both lines centered at $v \sim 0$ km s^{-1} . We find no significant velocity/redshift offset between the two components, indicating that they do not show any motion relative to

each other. This is also seen in the channel maps for the line core emission (Fig. 3), and in the moment-1 map (Fig. 4, panel b) which does not show a significant velocity gradient between A and B components.

The CO moment-0 map (Fig. 1) is created by integrating over the FWZI of the CO line. We fit the A and B component emission in the CO(1–0) moment-0 maps with 2D Gaussian components, and find velocity integrated line fluxes of $I_{\text{CO}}^{\text{A}} = 10.7 \pm 0.4$ Jy km s^{-1} and $I_{\text{CO}}^{\text{B}} = 1.8 \pm 0.1$ Jy km s^{-1} for components A and B, respectively. These correspond to CO line luminosities of $L'_{\text{CO,A}} = (8.4 \pm 0.3) \times 10^9$ $\text{K km s}^{-1} \text{ pc}^{-2}$ and $L'_{\text{CO,B}} = (1.4 \pm 0.1) \times 10^9$ $\text{K km s}^{-1} \text{ pc}^{-2}$, respectively. Assuming a CO-H₂ gas mass conversion factor $\alpha_{\text{CO}} = 0.8 M_{\odot} (\text{K km s}^{-1} \text{ pc}^{-2})^{-1}$, suitable for ULIRGs in the local universe (see Bolatto et al. 2013, for a review), we find total H₂ gas masses of $M_{\text{A}} = (6.7 \pm 0.2) \times 10^9 M_{\odot}$ and

Table 2. Photometry for IRAS 20100–4156 and IRAS 03158+4227.

Telescope	Band	$\lambda_{\text{eff}}(\mu\text{m})$	Aperture ^a	Flux (mJy)	Ref
IRAS 20100–4156					
GALEX	FUV	0.15	7".5	$(3.0 \pm 0.4) \times 10^{-2}$	(1)
	NUV	0.23	7".5	$(6.8 \pm 0.4) \times 10^{-2}$	(1)
HST	F814W	0.8	PF	(1.3 ± 0.1)	(2)
2MASS	J	1.24	20"	(2.3 ± 0.2)	(3)
	H	1.65	20"	(1.9 ± 0.4)	(3)
	Ks	2.17	20"	(2.8 ± 0.4)	(3)
WISE	W3	12	8".3	$(4.1 \pm 0.1) \times 10^1$	(4)
	IRS	11	3".7 ^b	$(6.7 \pm 0.4) \times 10^1$	(5)
Spitzer	IRS	13.5	3".7 ^b	$(3.1 \pm 0.1) \times 10^1$	(5)
	IRS	17	10".5 ^b	$(1.0 \pm 0.1) \times 10^2$	(5)
	IRS	23	10".5 ^b	$(4.1 \pm 0.1) \times 10^2$	(5)
	MIPS	24	PF	$(2.8 \pm 0.1) \times 10^2$	(6)
	IRS	26	10".5 ^b	$(8.3 \pm 0.1) \times 10^2$	(5)
	IRS	29	10".5 ^b	$(1.3 \pm 0.1) \times 10^3$	(5)
Herschel	cont.	64	45"	$(5.8 \pm 0.6) \times 10^3$	(7)
	cont.	78	45"	$(5.3 \pm 0.5) \times 10^3$	(7)
	cont.	84	45"	$(5.2 \pm 0.5) \times 10^3$	(7)
	cont.	120	45"	$(3.9 \pm 0.4) \times 10^3$	(7)
	cont.	131	45"	$(3.5 \pm 0.4) \times 10^3$	(7)
	cont.	146	45"	$(2.7 \pm 0.3) \times 10^3$	(7)
	cont.	158	45"	$(2.4 \pm 0.2) \times 10^3$	(7)
	cont.	169	45"	$(1.9 \pm 0.2) \times 10^3$	(7)
	SPIRE	250	17".6	$(1.0 \pm 0.1) \times 10^3$	(8)
	SPIRE	350	23".9	$(3.5 \pm 0.1) \times 10^2$	(8)
	SPIRE	500	35".2	$(1.2 \pm 0.3) \times 10^2$	(8)
ALMA	cont.	3.0×10^3	PF	(1.6 ± 0.3)	(2)
VLA	L band	2.1×10^5	PF	19.6 ± 4.0	(2)
IRAS 03158+4227					
SDSS	u'	0.35	PF	$(1.9 \pm 0.2) \times 10^{-2}$	(9)
	g'	0.48	PF	$(1.2 \pm 0.1) \times 10^{-1}$	(9)
	r'	0.62	PF	$(2.8 \pm 0.3) \times 10^{-1}$	(9)
	i'	0.76	PF	$(4.5 \pm 0.5) \times 10^{-1}$	(9)
	z'	0.91	PF	$(5.5 \pm 0.6) \times 10^{-1}$	(9)
Spitzer	IRS	11	3".7 ^b	(4.3 ± 0.9)	(5)
	IRS	13.5	3".7 ^b	$(4.4 \pm 0.2) \times 10^1$	(5)
	IRS	17	10".5 ^b	$(1.5 \pm 0.1) \times 10^2$	(5)
	IRS	23	10".5 ^b	$(4.9 \pm 0.1) \times 10^2$	(5)
	IRS	26	10".5 ^b	$(9.0 \pm 0.1) \times 10^2$	(5)
Herschel	IRS	29	10".5 ^b	$(1.4 \pm 0.1) \times 10^3$	(5)
	cont.	64	45"	$(4.9 \pm 0.6) \times 10^3$	(7)
	cont.	78	45"	$(4.9 \pm 0.5) \times 10^3$	(7)
	cont.	84	45"	$(4.8 \pm 0.5) \times 10^3$	(7)
	cont.	120	45"	$(3.1 \pm 0.4) \times 10^3$	(7)
	cont.	131	45"	$(2.9 \pm 0.4) \times 10^3$	(7)
	cont.	146	45"	$(2.7 \pm 0.3) \times 10^3$	(7)
	cont.	158	45"	$(2.2 \pm 0.2) \times 10^3$	(7)
	cont.	169	45"	$(2.1 \pm 0.2) \times 10^3$	(7)
	SPIRE	250	17".6	$(9.7 \pm 0.1) \times 10^3$	(8)
	SPIRE	350	23".9	$(3.8 \pm 0.1) \times 10^2$	(8)
	SPIRE	500	35".2	$(1.4 \pm 0.3) \times 10^2$	(8)
NOEMA	cont.	3.0×10^3	PF	$(9.5 \pm 0.1) \times 10^{-1}$	(2)
VLA	L band	2.1×10^5	PF	$(1.6 \pm 0.1) \times 10^1$	(2)

^aAperture for flux-extraction; PF stands for point-source fitting and extraction.

^bSlit width for IRS spectra.

References—(1) GALEX Data Release 6 Catalog (2) This work (3) 2MASS All Sky Survey, [Skrutskie et al. \(2006\)](#) (4) WISE All Sky Data Release (5) CASSIS, [Lebouteiller et al. \(2011, 2015\)](#) (6) *Spitzer*, [Capak et al. \(2013\)](#) (7) [González-Alfonso et al. 2017](#) (8) [Pearson et al. \(2016b\)](#) (9) SDSS DR IV, [Blanton et al. \(2017\)](#).

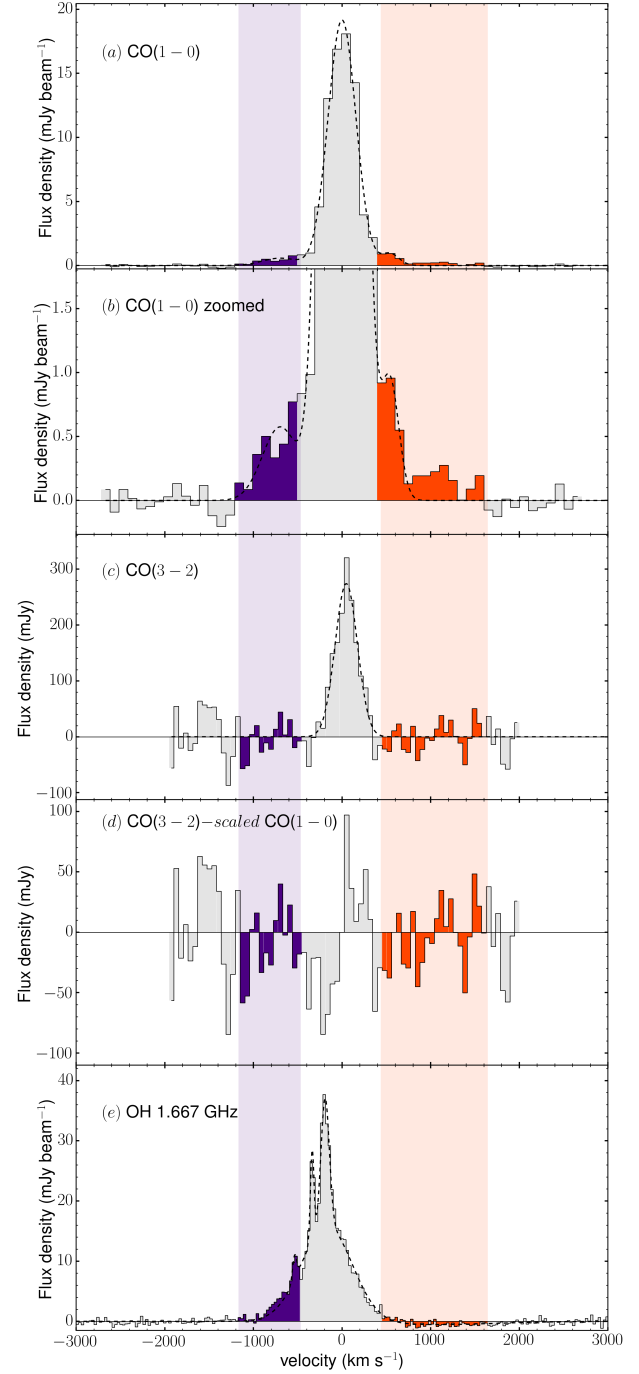


Figure 2. (a) CO(1–0) spectrum extracted from the peak pixel of component A in IRAS 20100–4156 (b) Same as (a), zoomed in to show the high-velocity outflow wings (c) CO(3–2) emission from IRAS 20100–4156 (d) Difference between CO(3–2) and scaled CO(1–0) line profiles. The CO(1–0) line profile has been binned and re-normalized to have the same spectral resolution and the same flux at $v \sim 0$ km s^{−1} as CO(3–2) (e) OHM spectrum for IRAS 20100–4156 extracted from the peak of OHM emission. The dashed lines show the sum of best fit Gaussians, using a combination of three Gaussians for (a) and (b), and four Gaussians for (e). The purple and orange regions show the velocity ranges for the blue and red outflow wings defined for the CO(1–0) spectrum (see § 3.1.2), and $v = 0$ km s^{−1} has been defined using z_{CO} . A systemic offset of $\Delta v \sim 190$ km s^{−1} between the peaks of the CO(1–0) and OHM line emission can be seen upon comparing (a) and (e).

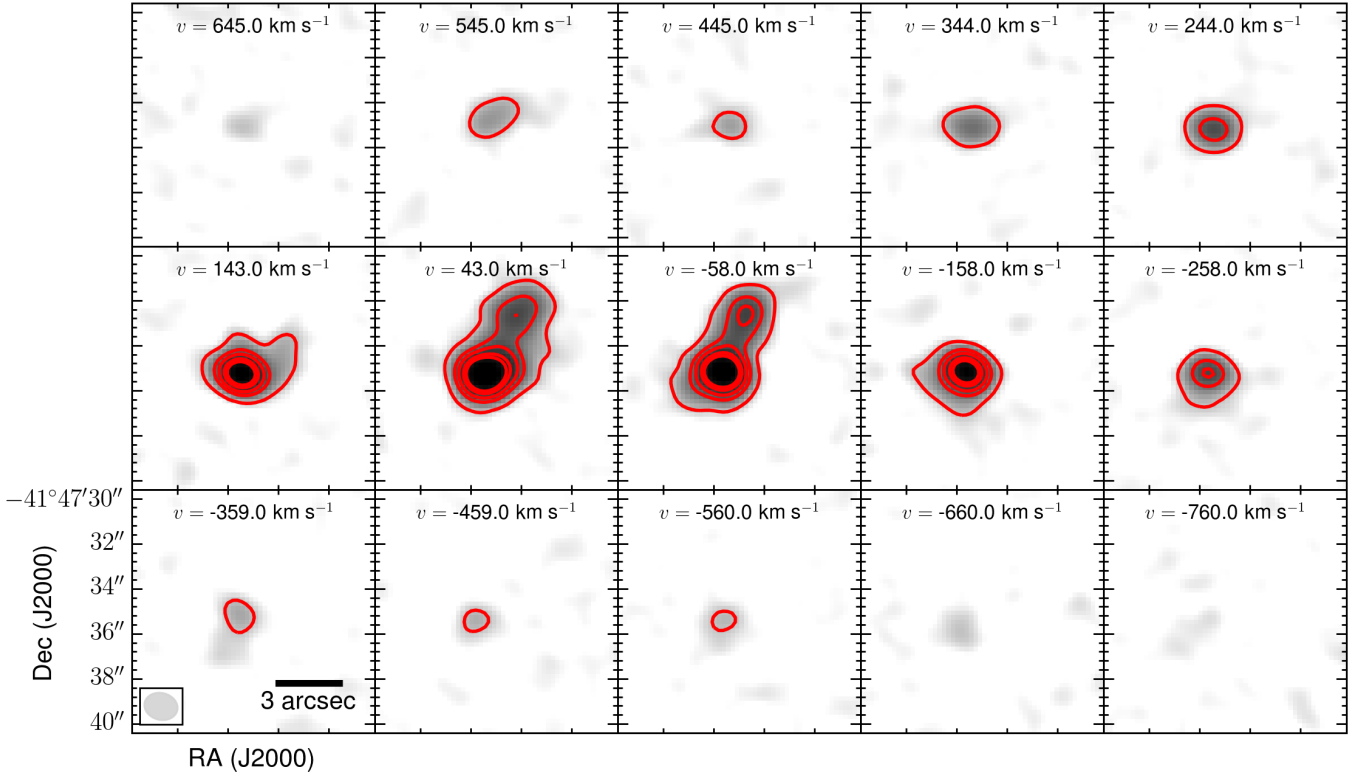


Figure 3. Channel maps for CO(1 – 0) emission from IRAS 20100–4156, at a velocity resolution of $\sim 100 \text{ km s}^{-1}$. Red contours represent the $\pm 7, 30, 50, 80, 100\sigma$ significance levels. The synthesized beam size is $1''.5 \times 1''.2$, and is shown on the bottom left. We spatially resolve the two merging components A and B, in the system, but we do not find a significant velocity offset between them.

$M_B = (1.1 \pm 0.1) \times 10^9 M_\odot$ for components A and B respectively.

We detect outflowing molecular gas from component A in the form of significant emission beyond $v \sim \pm 450 \text{ km s}^{-1}$ (Fig. 2), also seen in the position-velocity (PV) diagram (Fig. 4). We discuss the outflow wing emission in greater detail in the next section.

3.1.2. Determination of outflow wings

The determination of the outflow properties depends sensitively on the velocity widths (ranges) assumed for the high-velocity outflow wings, and we define the velocity ranges for outflow wings in an iterative manner. The initial spectrum is extracted from a $5'' \times 5''$ region centered on the peak pixel, and we simultaneously fit 3 Gaussian profiles to the spectrum, one each for the red wing, the blue wing and the line core, to avoid assumptions about the symmetry of the red and blue wings. The inner limits of the outflow velocity width are defined as the channel at which the wing emission starts dominating over the core emission, and the outer limits are defined using the fitted broad Gaussian components. The cleaned image cube is binned over these velocity ranges to obtain emission maps for the red and blue

wings, and CO spectra are re-extracted from the peak emission pixel in the red and blue emission maps. We again fit the obtained spectrum with a sum of 3 Gaussian components, and repeat the same procedure as above until it converges. We bin the calibrated and continuum subtracted uv -visibility data over the final velocity ranges, and use model fitting to the binned visibilities for the red and blue wings to determine the outflow positions and fluxes. We fit models to the binned visibility data using the CASA task UVMODELFIT, assuming a 2-D Gaussian source to obtain the FWHM spatial extent and the flux (see Appendix for details).

We find the velocity ranges for the red and blue outflow wings to be $\in (440, 1650) \text{ km s}^{-1}$ and $\in (-1169, -466) \text{ km s}^{-1}$, respectively. Based on uv model-fitting of the visibility data binned over these velocity ranges, we find integrated fluxes of $I_{\text{CO}}^{\text{red}} = 0.54 \pm 0.03 \text{ Jy km s}^{-1}$ and $I_{\text{CO}}^{\text{blue}} = 0.58 \pm 0.03 \text{ Jy km s}^{-1}$, and measure a velocity integrated line flux of $I_{\text{CO}}^{\text{core}} = 11.2 \pm 0.7 \text{ Jy km s}^{-1}$ in the line core. We find a projected spatial offset of $0''.9 \pm 0''.1$ between the peaks of the red and blue emission, which corresponds to a physical distance of $\sim 2.0 \pm 0.2 \text{ kpc}$ and which we define to be the outflow diameter (Table 3). The peaks of the red and blue wings are spatially

offset from the peak CO(1–0) and dust emission by $0''.3 \pm 0''.05$ and $0''.6 \pm 0''.1$, corresponding to physical distances of 0.7 ± 0.1 kpc and 1.4 ± 0.2 kpc respectively (Fig. 4). The resultant properties are consistent with those calculated from the cleaned image. The final velocity ranges and fluxes are given in Table 3. The outflow appears to be aligned with the velocity gradient seen across the galaxy (Fig. 4), although the velocity gradient is small between the peaks of the red and blue outflow wing. This raises the intriguing possibility that rotational support may play a role in the origin of the most powerful outflows (assuming that the outflow is in the plane of the galaxy; see González-Alfonso et al. 2017).

3.1.3. CO(3–2) emission

We detect CO(3–2) line emission at a $\sim 21\sigma$ significance from IRAS 20100–4156 (Fig. 2). The A and B components are spatially unresolved in the observations. Using a Gaussian fit to the observed spectrum, we find a linewidth of $\Delta v_{\text{FWHM}} = 293 \pm 25$ km s^{−1}. Integrating the line emission over the FWZI ($v \sim -269$ km s^{−1} to $v \sim 317$ km s^{−1}), we find an integrated flux of $I_{\text{CO}(3-2)} = 85.8 \pm 4.0$ Jy km s^{−1}. This corresponds to a line luminosity of $L'_{\text{CO}(3-2)} = (7.5 \pm 0.4) \times 10^9$ K km s^{−1} pc². Using the total observed CO(1–0) line luminosity (for both the A and B components combined), we find a brightness temperature ratio of $r_{31} \sim 0.8$, consistent with the mean ratio in other local ULIRGs ($\langle r_{31} \rangle \sim 0.7$, Papadopoulos et al. 2012).

We do not detect the high-velocity outflow wings seen in CO(1–0) in CO(3–2) emission at the depth of these observations. However, we tentatively find that while normalized line profiles for CO(3–2) and CO(1–0) agree at $v > 0$ km s^{−1}, they show a mismatch at $v < 0$ km s^{−1} (Fig. 2, d). This can be quantified using the line luminosity ratio $L'_{\text{CO}(3-2)}/L'_{\text{CO}(1-0)} = r_{31}$ for the red- and blue-shifted emission in the line core. We find $r_{31}^{\text{blue}} = 0.6 \pm 0.2$, while $r_{31}^{\text{red}} = 0.9 \pm 0.2$, where we have selected only those channels where CO(3–2) emission is detected at $\gtrsim 2\sigma$ significance. While both r_{31}^{red} and r_{31}^{blue} are consistent with the median r_{31} in ULIRGs, there is no physical reason for a difference in excitation between the red and blue-shifted emission. The observations can be explained if CO(3–2) emission is under-luminous on the blue-shifted side as compared to the redshifted emission. As the CO(3–2) emission traces more compact nuclear emission than CO(1–0), self-absorption in the molecular gas can result in decreased flux, leading to a lower r_{31}^{blue} than r_{31}^{red} . We therefore conclude that the average $r_{31} \gtrsim 0.8$, and treat it as a lower limit on the gas excitation.

3.1.4. OHM emission

We detect strong OHM emission from IRAS 20100–4156 at a $\sim 40\sigma$ significance. We detect line emission from a velocity range -927 km s^{−1} to 527 km s^{−1}, with tentative evidence of absorption redward of 527 km s^{−1} (Fig. 2). The OHM emission could be contaminated by the OH 1.665 GHz satellite line (OH $^2\Pi_{3/2}$, $J = 3/2, F = 1^e - 1^f$) at the expected position of $v \sim +360$ km s^{−1}, but we do not detect excess emission at that velocity. As the emission is spatially unresolved, we extract the spectrum from the peak pixel of the moment-0 map (Fig. 2). Based on a 2-D elliptical Gaussian fit to the moment-0 map, we find an integrated line flux of $I_{\text{OH}} = 27.9 \pm 0.8$ Jy km s^{−1}. This corresponds to a line luminosity of $L_{\text{OH}} = (1.5 \pm 0.1) \times 10^4 L_{\odot}$. We find a systematic velocity offset of $\delta v \sim 190 \pm 7$ km s^{−1} between the CO(1–0) and OHM lines, as well as a spatial offset of $0''.3 \pm 0''.1$ between the peaks of emission. We discuss these differences further in § 5.3.

3.2. IRAS 03158+4227

3.2.1. CO(1–0) emission

IRAS 03158+4227 is a merging system with two distinct galaxies spatially offset by $18''.9$, corresponding to 45.4 kpc ($1'' \sim 2.360$ kpc at $z = 0.13459$) as well as tidal structure with two components, one connecting the two galaxies. The two principal components are labeled A, B, while the two tidal components are labeled T and E (Fig. 5). We detect and spatially resolve the CO(1–0) line emission between each of these, and detect high-velocity outflowing molecular gas from component A (Fig. 6). We do not find a significant velocity offset between any of the components, as can be seen in the channels maps of the CO emission (Fig. 7), and the moment-1 map of the emission shows a relatively smooth velocity gradient across all components (Fig. 8). The moment-0 map of the CO emission is made by integrating over the FWZI line width (Fig. 5). The continuum emission, restricted to component A, has a flux of $f_{\lambda} = 0.94 \pm 0.03$ mJy at $\lambda_{\text{obs}} = 3$ mm, using the line-free channels.

The velocity widths and spatial extents of components A, B, T and E are significantly different. We therefore extract the fluxes for each component in the following iterative manner; we select a $3'' \times 3''$ region around the A, B and E components (and a $9'' \times 3''$ region around the elongated tidal tail T). We extract spectra from each of these regions, which is well described by a Gaussian line profile. Based on these spectra, we integrate over all contiguously positive channels around the line center to obtain a moment-0 map for each region. We then fit each component with a 2-D elliptical Gaussian, and

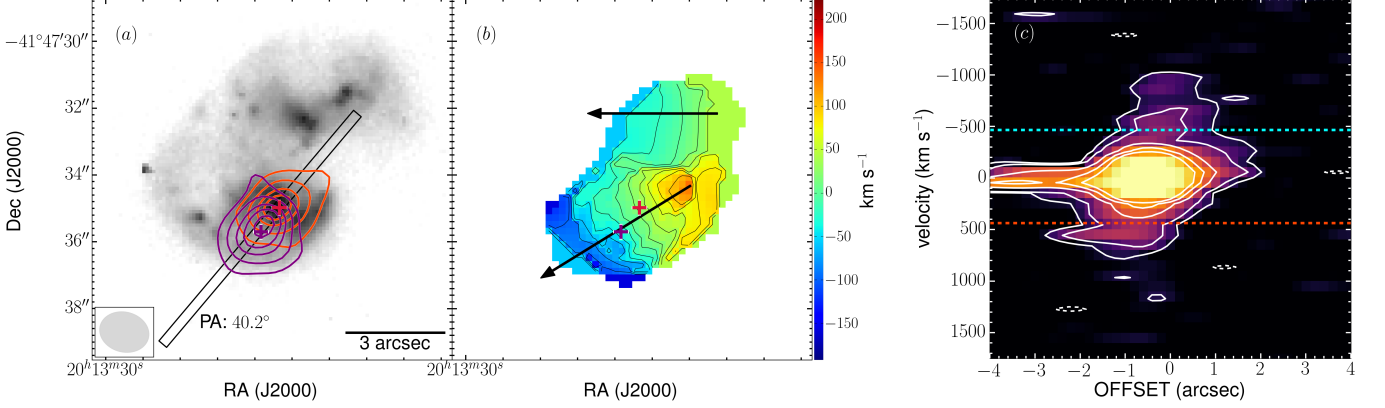


Figure 4. (a) $\pm 3, 6, 9, 11, 13\sigma$ significance contour levels for the red (shown in red) and blue (shown in purple) outflow emission in IRAS 20100–4156, overlaid on the HST/WFC2 814W image. The peaks of the red and blue outflow wing emission (marked by a red and purple cross, respectively) have a projected separation of $0''.9$ (~ 2 kpc) (b) The moment-1 map of the core of the CO(1–0) line emission ($-150 \text{ km s}^{-1} < v < 200 \text{ km s}^{-1}$), showing a relatively smooth velocity gradient across both components A and B in IRAS 20100–4156 (indicated by black arrows) the contours are marked at increments of 20 km s^{-1} from -140 to $+200 \text{ km s}^{-1}$. The red and blue outflow wings are nearly aligned with the galaxy-wide velocity gradient, though there is no significant velocity gradient between the peaks of the red and blue outflow wing positions (c) Position-velocity (PV) diagram from the region marked in black in (a), along an angle $\sim 40.2^\circ$; the dashed lines show the velocity limits beyond which we detect emission from the red and blue outflow wings. Component B is detected as the extended feature along $v \sim 0 \text{ km s}^{-1}$, with an offset up to $-4''$. The white contours show the $\pm 3, 7, 23, 40, 60\sigma$ significance levels.

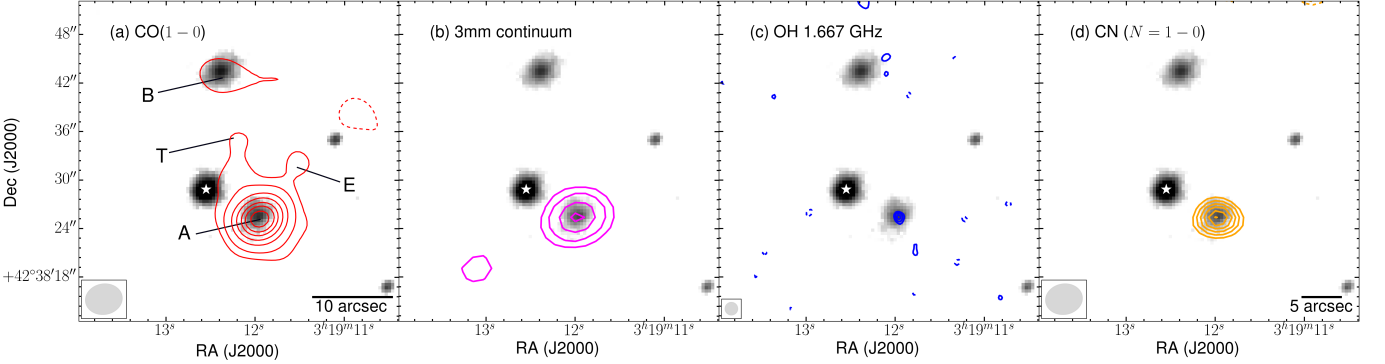


Figure 5. (a) Moment-0 map of CO(1–0) emission from IRAS 03158+4227, created by integrating over the velocity range ($-944, 1750$) km s^{-1} , overlaid on the SDSS g' band image (b) the 3mm continuum emission from IRAS 03158+4227 (c) Moment-0 map of the spatially unresolved OHM emission, created using the velocity range ($-1404, 296$) km s^{-1} . (d) Moment-0 map of the CN($N = 1 - 0$) emission, created using the velocity range ($-289, 429$) km s^{-1} . Panels (a) and (b) show contours marked at $\pm 3, 7, 15, 23, 32, 40, 50, 60, 80\sigma$ significance levels, while (c) and (d) show the contours at $\pm 3, 4, 5, 6, 7, 8\sigma$ significance levels. The peaks of the two components of the interacting pair (marked A and B) have a projected separation of $18''.9$ (45.4 kpc). We detect the molecular gas outflow from component A. Synthesized beam sizes are $4''.8 \times 3''.9$ for (a), (b), and (d) and $1''.6 \times 1''.3$ for (c), and are shown at the bottom left of each panel.

The white star shows the foreground star in the field of view.

thus extract the flux from each component - A, B, T and E. We iteratively fit and subtract emission from A, B and T, and find velocity integrated line fluxes of $I_{\text{CO}}^{\text{A}} = 13.1 \pm 0.1$, $I_{\text{CO}}^{\text{B}} = 2.8 \pm 0.3$, $I_{\text{CO}}^{\text{T}} = 2.1 \pm 0.4$ and $I_{\text{CO}}^{\text{E}} = 1.2 \pm 0.1 \text{ Jy km s}^{-1}$ respectively for each of the components. These imply line luminosities of $L'_{\text{CO,A}} = (1.1 \pm 0.1) \times 10^{10}$, $L'_{\text{CO,B}} = (2.4 \pm 0.2) \times 10^9$, $L'_{\text{CO,T}} = (1.8 \pm 0.4) \times 10^9$, and $L'_{\text{CO,E}} = (9.7 \pm 0.8) \times 10^8$

$\text{K km s}^{-1} \text{ pc}^{-2}$ respectively. Assuming a CO-luminosity to H_2 gas mass conversion factor of $\alpha_{\text{CO}} = 0.8 M_{\odot} (\text{K km s}^{-1} \text{ pc}^{-2})^{-1}$ for A and B, and a $\alpha_{\text{CO}} = 3.6 M_{\odot} (\text{K km s}^{-1} \text{ pc}^{-2})^{-1}$ for the tidal components, we find gas masses of $M_{\text{A}} = (8.9 \pm 0.8) \times 10^9$, $M_{\text{B}} = (1.9 \pm 0.2) \times 10^9$, $M_{\text{T}} = (6.3 \pm 1.3) \times 10^9$ and $M_{\text{E}} = (3.6 \pm 0.5) \times 10^9 M_{\odot}$, respectively. The differing conversion factors are physically motivated, with the lower conversion factor suit-

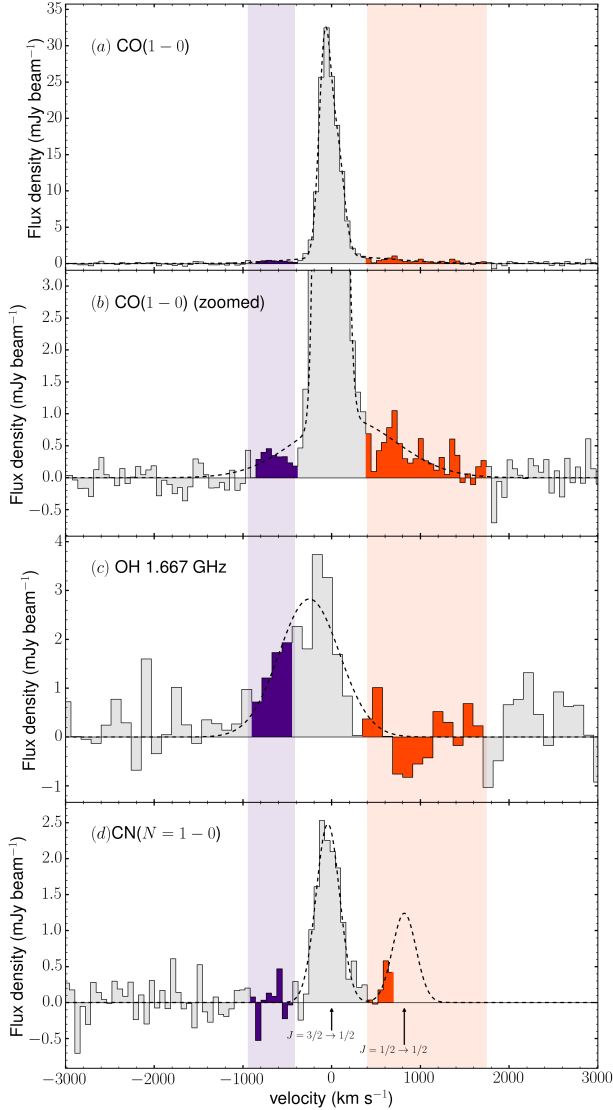


Figure 6. (a) CO(1 – 0) spectrum extracted from the peak pixel of component A, IRAS 03158+4227 (b) Same as (a), zoomed in to show the high-velocity wings (c) OHM spectrum for IRAS 03158+4227, extracted from the peak emission position (d) CN($N = 1 - 0$) spectrum for IRAS 03158+4227, with only the $J = 3/2 - 1/2$ component fully detected. The dashed line show the best fit spectra using a sum of three 1D Gaussian components for CO(1 – 0) and using a one-component Gaussian fit for OHM emission. For CN($N = 1 - 0$), the dashed line shows the expected line profile for the doublet, assuming LTE. The purple and orange regions show the velocity ranges for the high-velocity outflow wings in CO(1 – 0), defined in § 3.1.2, and $v = 0 \text{ km s}^{-1}$ has been defined using z_{CO} .

able for ULIRGs, which typically show higher gas temperatures, while the higher α_{CO} is more realistic for molecular gas in MW-type giant molecular clouds, and therefore is more suitable for the tidal tails. We find a gas-mass ratio of $\sim 5 : 1$ between the two principal

components A and B. We detect the high-velocity wing emission at velocities beyond $\pm 1000 \text{ km s}^{-1}$ in the PV diagram for IRAS 03158+4227 (Fig. 8).

3.2.2. Determination of outflow wings

We obtain the velocity widths for the outflow wings in the same manner as for IRAS 20100–4156 (see § 3.1.2), and find the velocity range $\in (400, 1750) \text{ km s}^{-1}$ as the red and $\in (-944, -413) \text{ km s}^{-1}$ as the blue outflow wings respectively, for IRAS 03158+4227. Based on uv model-fitting of the binned visibility data over this velocity range, we find integrated fluxes of $I_{\text{CO}}^{\text{red}} = 0.80 \pm 0.22 \text{ Jy km s}^{-1}$ and $I_{\text{CO}}^{\text{blue}} = 0.31 \pm 0.15 \text{ Jy km s}^{-1}$ in the red and blue wings respectively. We measure a total velocity integrated line flux of $I_{\text{CO}}^{\text{core}} = 8.4 \pm 0.7 \text{ Jy km s}^{-1}$ in the line core. We find a spatial offset of $1''.6 \pm 1''.1$ between the peaks of the red and blue emission, which corresponds to a physical distance of $3.9 \pm 2.7 \text{ kpc}$ (which we use as the outflow diameter). The peaks of the red and blue wings are spatially offset from the CO(1 – 0) and dust peaks by $0''.6 \pm 0''.2$ and $1''.1 \pm 0''.5$ respectively, corresponding to a physical distance of $\sim 1.4 \pm 0.4 \text{ kpc}$ and $\sim 2.6 \pm 1.2 \text{ kpc}$ (Fig. 8). The difference in the red and blue outflow peak offsets indicates a significant asymmetry in the outflow morphology. The outflow is counter-aligned with the galaxy-wide velocity gradient (Fig. 8), in direct contrast with that seen in IRAS 20100–4156. It is therefore unlikely that host galaxy rotation is an essential component in launching the outflows.

3.2.3. CN line emission

CN abundance is enhanced in UV-irradiated surfaces of molecular gas clouds, and therefore preferentially traces photo-dissociated regions (PDRs; Rodriguez-Franco et al. 1998), while CO traces the entirety of the molecular gas (dense as well as diffuse components). A low $L'_{\text{CO}}/L'_{\text{CN}}$ ratio therefore indicates relatively more PDR/XDR dominated molecular gas.

We detect CN($N = 1 - 0$) line emission from only component A in IRAS 03158+4227 Fig. 5. While the line is a doublet, with the fine structure (FS) components ($J = 1/2 - 1/2$) and ($J = 3/2 - 1/2$) separated by $\delta\nu_{\text{rest}} \sim 0.31 \text{ GHz}$, corresponding to $\delta v \sim 819 \text{ km s}^{-1}$, we cover only the ($J = 3/2 - 1/2$) component of the transition. Fitting a 1D Gaussian to the spectral line, we find a velocity width of $\Delta v_{\text{FWHM}} = 312.5 \pm 24.9 \text{ km s}^{-1}$, centered on $v_{\text{sys}} = -42.9 \pm 10.4 \text{ km s}^{-1}$. We create a moment-0 map by integrating over the FWZI velocity range ($v = -289 \text{ km s}^{-1}$ to $v = 429 \text{ km s}^{-1}$). Fitting the moment-0 emission with a 2-D Gaussian source, we find an integrated line flux of $I_{\text{CN}} = 1.0 \pm 0.1 \text{ Jy km s}^{-1}$. This corresponds to a line luminosity of $L'_{\text{CN}} = (8.9 \pm 0.5) \times 10^8 \text{ K km s}^{-1} \text{ pc}^{-2}$.

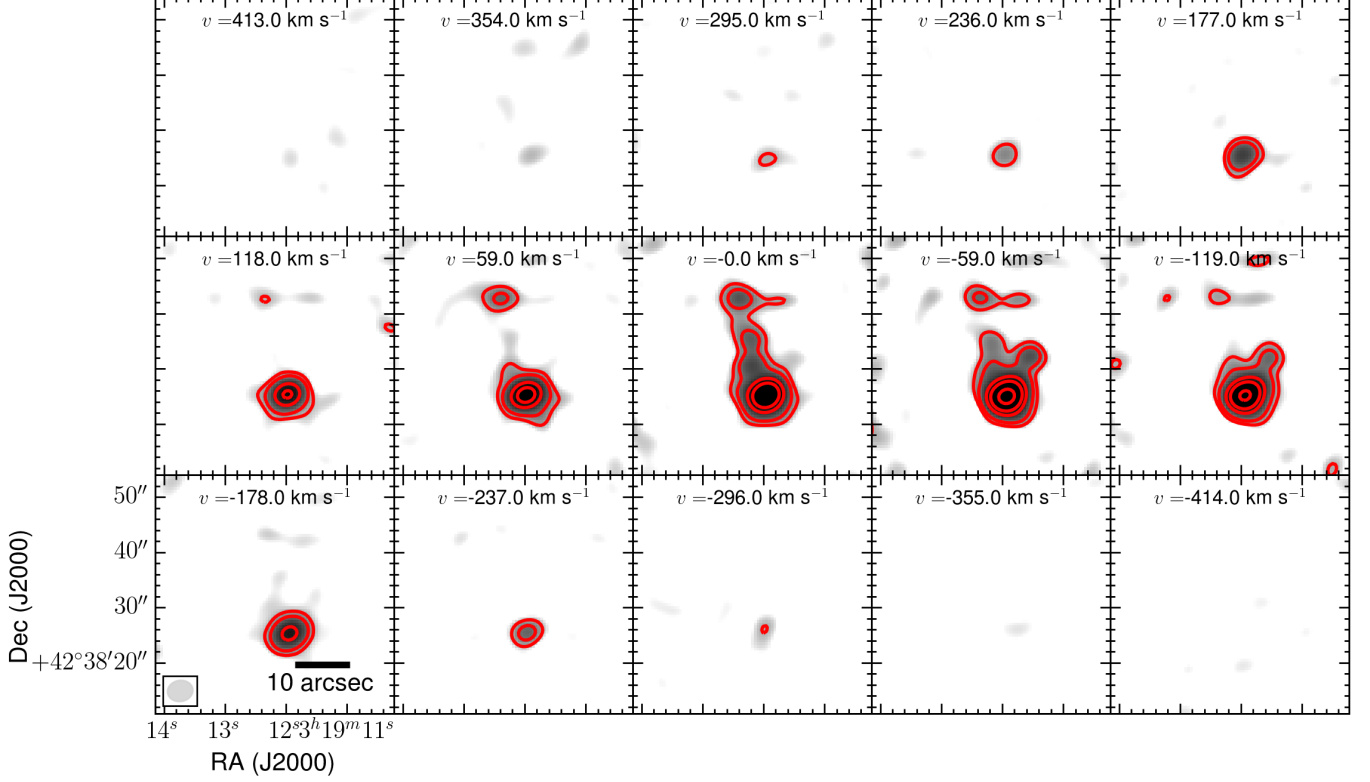


Figure 7. Channel maps for CO(1 – 0) emission from IRAS 03158+4227, with a velocity resolution of $\sim 60 \text{ km s}^{-1}$. The red contours represent the $\pm 7, 30, 50, 80, 100\sigma$ significance levels. The synthesized beam size is $4''.8 \times 3''.9$, and is shown on the bottom left. We spatially resolve multiple components of the merging system - A, B, T and E, and note that there is no significant velocity offset between these components.

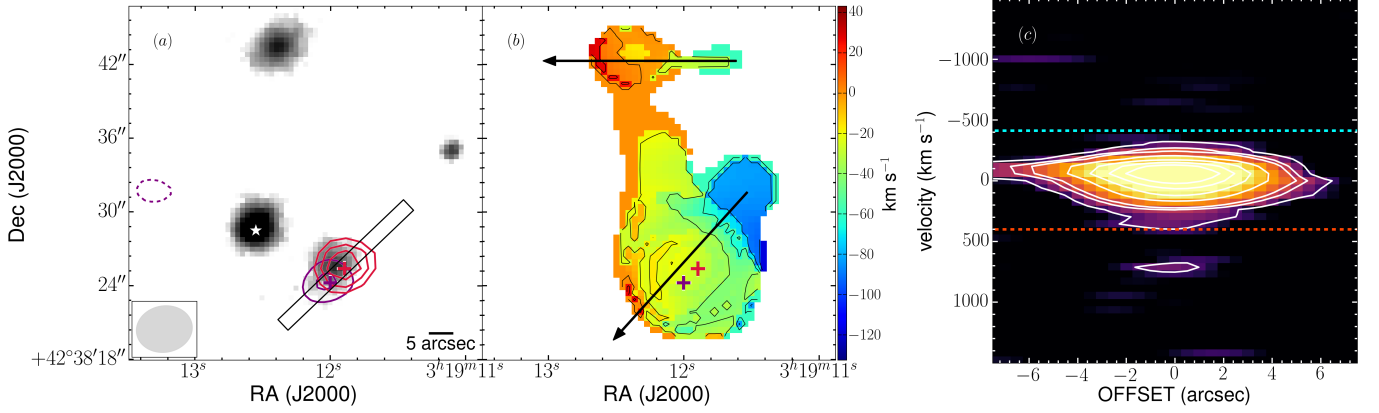


Figure 8. (a) $\pm 3, 6, 9, 11, 13\sigma$ significance contour levels for the red (shown in red) and blue (shown in purple) outflow emission in IRAS 03158+4227, overlaid on the SDSS g' band image. The peaks of the red and blue outflow wing emission (marked by a red and purple cross, respectively) have a projected separation of $1''.6$ ($\sim 3.9 \text{ kpc}$) (b) The moment-1 map of the core of the CO(1 – 0) line emission ($-120 \text{ km s}^{-1} < v < 40 \text{ km s}^{-1}$), which shows distinct velocity gradients along both components A and B, as shown by the arrows in each; the contours are marked at increments of 20 km s^{-1} from -120 to $+120 \text{ km s}^{-1}$ (c) The PV diagram extracted from the region marked in (a), along an angle $\sim 46^\circ$; the dashed lines show the velocity ranges for the red and blue outflow wings, as defined in § 3.1.2. The peaks of the red and blue outflow wing emission are nearly anti-aligned with the large scale rotation of the galaxy (indicated by black arrows for both component A and B), though there is no significant velocity gradient between the peaks of the red and blue outflow wing positions. Component E is detected as the extended feature detected along $v \sim 0 \text{ km s}^{-1}$. The white contours show the $\pm 3, 7, 10, 23, 40, 60\sigma$ significance levels.

Under conditions of Local Thermal Equilibrium (LTE) between the two FS components, we expect that the two components will have a ratio of

$$R_{12}\text{CN}(N=1-0) = \frac{I(J=1/2-1/2)}{I(J=3/2-1/2)} = 0.5 \quad (1)$$

The expected line profile of the doublet in LTE is shown in Fig. 6. While the $\text{CN}(N=1-0, J=3/2-1/2)$ and $(N=1-0, J=1/2-1/2)$ lines are split further into hyperfine structure lines (HFS), we do not spectrally resolve them. Assuming LTE, we find an expected integrated line flux of $I_{\text{CN}} = 1.5 \pm 0.2 \text{ Jy km s}^{-1}$ for both components together, corresponding to a line luminosity of $L'_{\text{CN}} = (1.3 \pm 0.1) \times 10^9 \text{ K km s}^{-1} \text{ pc}^{-2}$. Using the $\text{CO}(1-0)$ line luminosity as calculated above, we find a line luminosity ratio of $L'_{\text{CO}}/L'_{\text{CN}} \sim 8.2 \pm 0.5$. The observed $L'_{\text{CO}}/L'_{\text{CN}}$ is consistent with the globally averaged line-ratios seen in other ULIRGs and is similar to that seen in Mrk 231 ($L'_{\text{CO}}/L'_{\text{CN}} \sim 8$, Aalto et al. 2002; Pérez-Beaupuits et al. 2007). With a critical density 5 times lower than $\text{HCN}(1-0)$, $\text{CN}(N=1-0)$ does not trace the same molecular gas as HCN, and $L'_{\text{HCN}}/L'_{\text{CN}}$ varies in the range $\sim 0.5-6$ for galaxies with a constant $L'_{\text{CO}}/L'_{\text{HCN}}$ (Aalto et al. 2002). We therefore do not use it to calculate the dense gas mass.

3.2.4. OHM emission

We detect spatially unresolved OHM emission from component A of IRAS 03158+4227 (Fig. 6). Fitting a 1D Gaussian to the spectral line profile, we find a velocity width of $\Delta v_{\text{FWHM}} \sim 803 \pm 110 \text{ km s}^{-1}$, and a velocity offset of $v_0 \sim -252 \pm 46 \text{ km s}^{-1}$ between the CO and OHM lines. Based on a 2-D elliptical Gaussian fit to the moment-0 map (Fig. 5), we find an integrated line flux of $I_{\text{OH}} = 4.1 \pm 0.8 \text{ Jy km s}^{-1}$. This corresponds to a line luminosity of $L_{\text{OH}} = (2.4 \pm 0.5) \times 10^3 L_{\odot}$. We detect a marked asymmetry in the maser emission line profile, with a significant excess in the blueshifted emission, similar to that observed in the OHM spectrum for IRAS 20100–4156. This is discussed further in § 5.3.

4. ANALYSIS

4.1. Outflow properties

The physical properties of outflows can be encapsulated by the mass outflow rate \dot{M}_{OF} , the momentum outflow flux \dot{P}_{OF} , and the kinetic flux $\dot{E}_{\text{kin,OF}}$ of the outflowing gas, and the use of all three is important to distinguish between different outflow models². These are defined as

$$\dot{M}_{\text{OF}} = v_{\text{OF}} \Omega R_{\text{OF}}^2 \rho_{\text{OF}} \quad (2)$$

$$\dot{P}_{\text{OF}} = v_{\text{OF}} \dot{M}_{\text{OF}} \quad (3)$$

$$\dot{E}_{\text{kin,OF}} = \dot{M}_{\text{OF}} v_{\text{OF}}^2 / 2 \quad (4)$$

where \dot{M}_{OF} is the mass outflow rate, v_{OF} is the outflow velocity, R_{OF} is the outflow radius, Ω is the solid angle of the outflow (4π steradians for a spherical outflow) and ρ_{OF} is the density of the outflowing material at R_{OF} . In the case of a spherical outflow of radius R_{OF} uniformly filled with outflowing clouds, assuming that $\rho_{\text{OF}} \sim \rho_{\text{avg}}/3$ (where ρ_{avg} is the average density of the outflowing gas), and that the mass in the outflow is $M_{\text{OF}} = (\Omega/3) R_{\text{OF}}^3 \rho_{\text{avg}}$, the mass outflow rate \dot{M}_{OF} in steady state is given by

$$\dot{M}_{\text{OF}} = M_{\text{OF}} \frac{v_{\text{OF}}}{R_{\text{OF}}} \quad (5)$$

However, for a thin shell-like geometry of the outflow, the volume density is given by

$$\rho_{\text{OF}} = \frac{3M_{\text{OF}}}{\Omega(R_{\text{in}}^3 - R_{\text{OF}}^3)} \approx \frac{M_{\text{OF}}}{\Omega R_{\text{OF}}^2 \Delta R} \quad (6)$$

where R_{in} and R_{OF} are the inner and outer radii of the outflowing shell, and ΔR is the thickness of the shell. In this geometry, the mass outflow rate \dot{M}_{OF} is given by

$$\dot{M}_{\text{OF}} = M_{\text{OF}} \frac{v_{\text{OF}}}{\Delta R} \quad (7)$$

Note that the outflow solid angle is included in M_{OF} , and thus Equation 7 holds for spherical as well as bi-conical outflows. The thin shell case implies higher outflow rates, as ΔR is smaller than R_{OF} . This can also be thought of as the instantaneous estimate of the energetics, valid over timescales $\Delta \tau \sim \Delta R/v_{\text{OF}}$; the time-average of this expression yields the same expression as the steady-state case described above; González-Alfonso et al. 2017). In order to distinguish between these two cases observations with a higher spatial resolution (at least $\sim 100 \text{ pc}$) are required. We therefore calculate the outflow properties assuming the first model (Equation 5). This is consistent with the formalism adopted in Heckman et al. (2015); Thompson et al. (2015); González-Alfonso et al. (2017), but is a factor of 3 lower than the values assumed in Feruglio et al. (2010); Maiolino et al. (2012); Ciccone et al. (2014); García-Burillo et al. (2015). The decreasing density as a function of radius assumed in the model used is also consistent with observations that outflowing dense gas is more spatially compact than ground-state CO emission (Feruglio et al. 2015).

² All outflow properties are identified with a subscript OF

We obtain outflowing gas masses using α_{CO} to convert between the line luminosity and the gas mass, assuming $\alpha_{\text{CO}} \sim 0.8 M_{\odot} (\text{K km s}^{-1} \text{ pc}^{-2})^{-1}$ to calculate the outflow mass (a typical value for ULIRGs), and assuming that the outflowing gas is 100% molecular. The value of α_{CO} can be lower by a factor of ~ 2.4 or higher by a factor of ~ 5.5 , depending on the two limiting cases of optically thin molecular gas $\alpha_{\text{CO}} = 0.34 M_{\odot} (\text{K km s}^{-1} \text{ pc}^{-2})^{-1}$, vs the upper limit of a MW-like $\alpha_{\text{CO}} = 4.3 M_{\odot} (\text{K km s}^{-1} \text{ pc}^{-2})^{-1}$ (see Bolatto et al. 2013, for a review). In fast moving winds/outflows, CO emission is expected to be optically thin i.e. $\alpha_{\text{CO}} \gtrsim 2\times$ lower than our assumed value, which has been seen in radio-jet driven molecular outflows (Oosterloo et al. 2017). α_{CO} could also be low if the outflowing molecular gas (which is mass-loaded early in the outflow; González-Alfonso et al. 2017) is enriched by the nuclear starburst and/or by *in situ* star formation in the outflow (Maiolino et al. 2017). However, observations of the CO excitation in Mrk 231 find the excitation in the outflowing gas to be similar to that seen in the bulk of the molecular gas, arguing for a similar α_{CO} in the outflow and the rest of the galaxy (Cicone et al. 2012). Theoretical modeling of the multi-phase ISM in outflows by Richings & Faucher-Giguere (2017a,b) suggests that the outflowing gas could have α_{CO} as much as 5.3 times lower than our assumed value. However, they also assume a molecular gas fraction of $\sim 20\%$ instead of 100%, and the two assumptions together cancel out to give an α_{CO} close to our adopted value (within $\sim 10\%$). However, we emphasize that there is a systematic uncertainty in the outflow mass, momentum flux, and energy flux due to α_{CO} , and further observations of isotopologues such as ^{13}CO are urgently needed to determine its appropriate value. We use the mass-weighted outflow velocity, averaged between the red and blue outflow wings, as the representative outflow velocity v_{OF} . We do not correct for inclination effects so as to get the most conservative outflow properties; \dot{M}_{OF} is independent of inclination, while both \dot{P}_{OF} and $\dot{E}_{\text{kin,OF}}$ are lower limits. We assume the radius of the outflow (R_{OF}) to be half the separation of the peaks of the red and blue emission peak, as described in § 3.1.2, § 3.2.2. We define the molecular gas depletion timescale to be $\tau_{\text{OF}}^{\text{dep}} = M_{\text{gas}}/\dot{M}_{\text{OF}}$, assuming that the outflow rate remains constant. The final outflow properties are listed in Table 4.

4.2. Determining the AGN luminosity

Both outflow sources are highly IR luminous ($L_{\text{IR}} > 10^{12} L_{\odot}$), with the bulk of the IR luminosity emerging from their compact, dust-obscured nuclei. Identifying what fraction of this IR luminosity is due to the AGN

or the compact nuclear starburst is essential for testing observed outflow parameters against theoretical models for the same. We therefore use Spectral Energy Distribution (SED) fitting, mid-IR diagnostics, and archival X-ray observations to determine L_{AGN} . The caveats to all these are discussed in § 4.2.5.

4.2.1. SED fitting

We perform Spectral Energy Distribution (SED) fitting for both sources using CIGALE (Code Investigating GALaxy Emission; Noll et al. 2009; Serra et al. 2011). CIGALE builds galaxy SEDs from UV to radio wavelengths assuming a combination of modules and summing the emission from each, and allows modeling the star formation history (SFH), the stellar emission using population synthesis models (Bruzual & Charlot 2003; Maraston 2005), nebular lines, dust attenuation (e.g., Calzetti et al. 2000), dust emission (e.g., Draine & Li 2007; Casey 2012), contribution from AGN (Dale et al. 2014; Fritz et al. 2006), and radio synchrotron emission. The SEDs implicitly maintain the energy budget, with consistency between UV dust attenuation and the dust emission. For our SED fitting, we assume the star formation history to be a double exponentially decreasing function of time, the dust attenuation as in Calzetti et al. (2000), and the dust emission models from Draine et al. (2014).

We use all available photometric data points (Table 2) for each of the sources³ as described in Section § 2.3. We add multiple line-free continuum points from the IRS spectra/PACS spectroscopy to our SED fitting, to ensure consistency between the spectroscopic and the SED fit observations.

The photometry resolves the targets and their merging/interacting companions in some cases, and not in others. For IRAS 20100–4156, the A and B components are not dynamically independent and are only spatially resolved in the HST images. We therefore treat them as one system. We re-extract HST photometry so as to include the contribution from both A and B components, and then perform the SED fitting. Based on the modest detection of the 3 mm dust continuum from the component B, we expect that the bulk of the FIR emission is from component A. For IRAS 03158+4227, the A and B components are separated by a projected distance of $\sim 22''$ and spatially resolved in all images except *Herschel* SPIRE photometry. We therefore perform the SED fitting for A with and without the SPIRE photometry, to test for contamination from component

³ We exclude the IRAC 3.6 - 8 μm photometry for IRAS 03158+4227 as the IRS map shows a mispointing.

B, and find no significant differences in our results. The near-IR wavelengths for IRAS 03158+4227 ($< 6 \mu\text{m}$) also show contamination from its neighboring star, and we re-extract the photometry where possible. Finally, CIGALE performs a probability distribution function analysis for our specified module parameters and obtains the likelihood-weighted mean value for each. The best-fit SED models are shown in Fig. 9.

We test for any AGN contribution to the SEDs using the Fritz et al. (2006) module, which includes AGN emission reprocessed by a dusty torus, with the torus opening angle, orientation, inner and outer radii being free parameters (see Fritz et al. 2006 for further details). We extensively test for AGN contributions to the IR luminosity by varying the initial conditions over the entire allowed parameter space for dusty torus models. We find bolometric AGN luminosities of $L_{\text{AGN}} = (7.2 \pm 0.3) \times 10^{11} L_{\odot}$ and $L_{\text{AGN}} = (1.3 \pm 0.1) \times 10^{12} L_{\odot}$ for IRAS 20100–4156 and IRAS 03158+4227, and $L_{\text{IR}} = 3.7 \times 10^{12} L_{\odot}$ and $L_{\text{IR}} = 3.8 \times 10^{12} L_{\odot}$. Together these correspond to AGN fractions of $f_{\text{AGN}} = 0.2 \pm 0.1$ and $f_{\text{AGN}} = 0.3 \pm 0.1$ for IRAS 20100–4156 and IRAS 03158+4227, respectively, indicating that neither of the sources is AGN-dominated. The final parameters estimated from the SED fitting - SFR, dust mass, and stellar mass - are listed in Table 5.

We find a gas to dust mass ratio $\delta_{\text{GDR}} \sim 10\text{--}20$ for both IRAS 20100–4156 and IRAS 03158+4227. Previous values for δ_{GDR} in (U)LIRGs calculated using galaxy-wide SED fitting to obtain the dust mass are similarly low ($\delta_{\text{GDR}} \sim 8\text{--}20$; Papadopoulos et al. 2010). These values are significantly smaller than those observed in nearby normal, star-forming galaxies ($\delta_{\text{GDR}} \sim 100\text{--}200$, Rémy-Ruyer et al. 2014). In addition, such low δ_{GDR} values are hardly consistent with the strong far-IR molecular absorption observed in the far-IR (e.g. González-Alfonso et al. 2015), which favor MW-like values with molecular abundances consistent with chemical models (González-Alfonso et al. 2018). Furthermore, spatially resolved observations of nuclear regions in (U)LIRGs also show MW-like high δ_{GDR} (e.g. Wilson et al. 2008), instead of the extremely low values inferred in ULIRGs.

This apparent contradiction is due to the degeneracy between the dust optical depth and the dust temperature. Emission from dust that is optically thick up to far-IR or sub-mm wavelengths (e.g. Sakamoto et al. 2008; González-Alfonso et al. 2015) naturally leads to excess FIR/sub-mm emission, and can dominate the emission from the cold dust component, leading to an overestimate of the dust mass. Distinguishing between these two cases is only possible with spatially resolved obser-

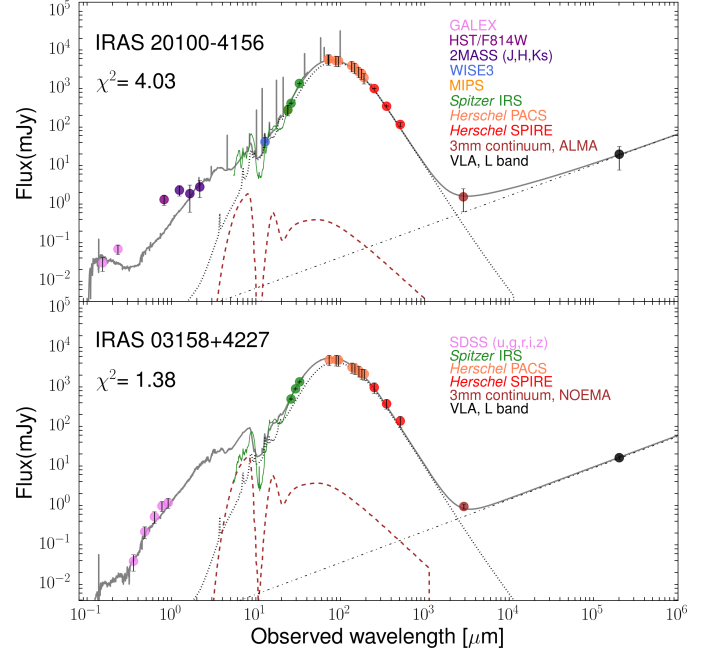


Figure 9. Best-fit Spectral Energy Distributions (SEDs) for IRAS 20100–4156 and IRAS 03158+4227 obtained using CIGALE. The solid grey line shows the overall best fit, the dotted line shows the dust emission SED, the dashed brown line shows the AGN emission, the dash-dotted line shows the radio continuum, and the green line shows the observed *Spitzer* IRS spectra.

vations of the dust continuum in the long wavelength, optically thin regime.

4.2.2. Mid-IR decomposition

Mid-IR spectroscopy offers a powerful way to determine the AGN fraction even in dust-obscured nuclei, as the blackbody emission from AGN-heated dust at $T \sim 1000\text{--}1500$ K at the inner boundary of the dust torus (the dust sublimation temperature) within ~ 10 pc of the AGN peaks in the mid-IR. For IRAS 20100-4156 and IRAS 03158+4227, we do not detect broad-line signatures in optical/near-IR/mid-IR spectra, suggesting that we are looking at the torus edge-on. We calculate the AGN fraction using the method developed in Nardini et al. (2008), based on the observation that the relative difference between mid-IR spectra of AGN and starburst dominated galaxies is the highest in the $5\text{--}8 \mu\text{m}$ regime. The $5\text{--}8 \mu\text{m}$ mid-IR spectra of starburst galaxies are fairly consistent (Brandl et al. 2006), and are dominated by emission from Polycyclic Aromatic Hydrocarbon (PAH) features at $6.2 \mu\text{m}$ and $7.7 \mu\text{m}$, while those of AGN dominated galaxies show a smooth power-law continuum emission. PAH features are associated with star formation activity, as they exist in photodissociation regions and HII regions, and are de-

stroyed in the intense radiation fields surrounding an AGN (e.g. Genzel et al. 1998; Laurent et al. 2000). The mid-IR spectra of ULIRGs can therefore be decomposed into their AGN and starburst components in the following manner

$$f_{\nu}^{\text{obs}} = f_{\nu}^{\text{int}}[(1 - \alpha_6)u_{\nu}^{\text{SB}} + \alpha_6 u_{\nu}^{\text{AGN}} e^{-\tau(\lambda)}] \quad (8)$$

where f_{ν}^{obs} is the observed flux, f_{ν}^{int} is the intrinsic flux density, u_{ν}^{SB} and u_{ν}^{AGN} are the SB and AGN templates, normalized at $6\mu\text{m}$, α_6 is the fraction of the flux contributed by the AGN at $6\mu\text{m}$, and the PAH features are automatically included in the SB template. We include the dust extinction in the form of $\tau(\lambda) \propto \lambda^{-1.75}$ (Draine & Li 2007). There are additional features detected in the mid-IR spectra of ULIRGs, such as the $6\mu\text{m}$ water-ice absorption, and additional aliphatic hydrocarbon (HAC) features at 6.85 and $7.25\mu\text{m}$. We include the $6\mu\text{m}$ water-ice feature using the 15-K pure water-ice spectrum from the Leiden ice database⁴, and model the $6.85\mu\text{m}$ and $7.25\mu\text{m}$ aliphatic hydrocarbon features as Gaussians. We apply these to the fitting by adding additional multiplicative terms to Equation 8. We create the starburst template by averaging the mid-IR spectra from five starburst-dominated ULIRGs, IRAS 10190+1322, IRAS 12112+0305, IRAS 17208-0014, IRAS 20414-1651 and IRAS 22491-1808 (all with $f_{\text{AGN}} \lesssim 0.05$, using multi-band observations in the literature), and use a power-law template for the AGN contribution ($f_{\nu} \propto \lambda^{\gamma}$, with $\gamma \sim 0.7 - 1.5$). We leave the parameters for the ice features, α_6 , the optical depth at $6\mu\text{m}$ and the overall normalization as free parameters in the fitting. We extrapolate from the α_6 to f_{AGN} , the AGN contribution to the bolometric luminosity i.e. $L_{\text{AGN}} \sim f_{\text{AGN}} L_{\text{IR}}$, and thus the AGN luminosity L_{AGN} (see Nardini et al. 2008, 2010, for more details). The best-fit mid-IR decompositions for IRAS 20100-4156 and IRAS 03158+4227 are shown in Fig. 10. We find that the best-fit model deviates from the observed mid-IR emission at $5-5.5\mu\text{m}$, and finds a shallower slope in that spectral range than is actually observed. The steeper slope observed is likely due to the extended $4-5\mu\text{m}$ CO gas/ice absorption feature (see Spoon et al. 2004), which we have not included in our modeling. We find AGN fractions of $f_{\text{AGN}} = 0.14 \pm 0.47$ and $f_{\text{AGN}} = 0.43 \pm 0.18$ for IRAS 20100-4156 and IRAS 03158+4227, respectively. These are consistent within the uncertainties with f_{AGN} found using SED fitting (§ 4.2.1), and also consistent with the AGN fractions found previously for these objects; Nardini et al. 2009,

and those typically found in ULIRGs (Farrah et al. 2012).

To enable comparison between IRAS 20100-4156, IRAS 03158+4227, and other molecular outflows detected using CO in ULIRGs, we have compiled all such sources from the literature (Cicone et al. 2014; García-Burillo et al. 2015; Veilleux et al. 2017), and also performed a similar mid-IR decomposition for them. We find results generally consistent with previous AGN fractions for those sources included in the Cicone et al. (2014) sample⁵. The results of all these are shown in Table 4.

4.2.3. Comparison of AGN diagnostics against X-ray observations.

We compare L_{AGN} from mid-IR spectral decomposition to the previously obtained L_{AGN} from X-ray observations for our two sources. Primary hard X-ray spectra from AGN are characterized by an X-ray photon index Γ (where the number of photons at energy E is given by $n(E) \propto E^{-\Gamma}$), with the power-law cutoff energy determined by the column density N_{H} , and increasing to higher photon energies at higher column densities. In addition to this, X-ray spectra from AGN-dominated ULIRGs also show a broad Fe K- α line at 6.4 keV , with equivalent width $\text{EW} \sim 1\text{ keV}$. The soft X-ray emission ($\lesssim 1\text{ keV}$) is often dominated by thermal emission from a hot plasma at $\sim 0.7\text{ keV}$ from nuclear starburst activity. While primary hard-X ray emission from the AGN may be blocked at energies $< 10\text{ keV}$ in deeply obscured Compton thick sources ($N_{\text{H}} \gtrsim 1.5 \times 10^{24}\text{ cm}^{-2}$), spectra up to 10 keV can be used to determine the power-law cutoff (which gives the column density), the Fe K- α line, and reflection components, depending on the geometry of the absorber.

For IRAS 20100-4156, XMM-Newton was used to observe the $0.5-10\text{ keV}$ X-ray emission (Franceschini et al. 2003). The emission was detected at modest significance, and the spectrum modeled using a combination of thermal plus a power-law emission (either absorbed or with a cut-off, both similarly good fits). The photon indices were fixed to $\Gamma \sim 1.1$ and $\Gamma \sim 1.7$, and both fits gave comparable values for $N_{\text{H}} \sim 2 - 2.3 \times 10^{22}\text{ cm}^{-2}$, and intrinsic absorption-corrected $2-10\text{ keV}$ luminosity of $L_{2-10\text{ keV}} = 1.6 \times 10^{42}\text{ ergs s}^{-1}$ i.e. IRAS 20100-4156 does not show AGN-dominated X-ray emission. AGN-host galaxies also show a relative FIR deficit (or X-ray excess) in the X-ray - L_{FIR} relation (Ranalli et al. 2003; Franceschini et al. 2003). IRAS 20100-4156

⁴ <http://icedb.strw.leidenuniv.nl/>

⁵ Our values are within 0.1 dex for all such sources, except for IRAS 10565+2448, for which we find an $f_{\text{AGN}} \sim 0.05$, while $f_{\text{AGN}} \sim 0.17$ in the literature.

is consistent within the scatter in this relation, showing that the observed X-ray emission is predominantly from starburst activity.

However, we note that the obtained column density is lower than the column density obtained from modeling of far-IR OH lines (González-Alfonso et al. 2017), which is $> 10^{24} \text{ cm}^{-2}$. It is then possible that IRAS 20100–4156 hosts an intrinsically X-ray weak and deeply obscured AGN, which is drowned out by the X-ray emission from less obscured circumnuclear starburst. Such X-ray weak AGN have been seen in local ULIRGs (including Mrk 231, Teng et al. 2014, 2015) and have been attributed to super-Eddington accretion onto the central SMBH (Vasudevan & Fabian 2009; Lusso et al. 2010, 2012).

A similar lack of X-ray AGN signatures is found for IRAS 03158+4227. The Advanced Satellite for Cosmology and Astrophysics (ASCA) was used to observe the hard X-ray emission in IRAS 03158+4227 and detected a $2 - 10 \text{ keV}$ flux of $\sim (5.4 \pm 1) \times 10^{-13} \text{ ergs s}^{-1} \text{ cm}^{-2}$ (Risaliti et al. 2000). This implies a $2 - 10 \text{ keV}$ luminosity of $L_{2-10\text{keV}} = (2.5 \pm 0.5) \times 10^{43} \text{ ergs s}^{-1}$, consistent with thermal emission, though Risaliti et al. (2000) invoke high column densities of $N_{\text{H}} > 10^{24} \text{ cm}^{-2}$ to explain the lack of X-ray AGN signatures. We also note that the ASCA field of view is $50'$, and the detected emission is likely contaminated by the interacting companion of IRAS 03158+4227, which is a Seyfert 1 galaxy (Meusinger et al. 2001).

Overall we do not find X-ray signatures for AGN in either IRAS 20100–4156 and IRAS 03158+4227. We convert between $L_{2-10\text{keV}}$ and the bolometric AGN luminosity using relations from Marconi et al. (2004), and find $L_{\text{AGN}} \sim 2 \times 10^{10} L_{\odot}$ and $L_{\text{AGN}} \sim 3 \times 10^{11} L_{\odot}$, which correspond to $f_{\text{AGN}} \sim 0.005$ and $f_{\text{AGN}} \sim 0.08$ for IRAS 20100–4156 and IRAS 03158+4227 respectively. The ratios of the $L_{2-10\text{keV}}$ to the bolometric AGN luminosity are then 0.08% and 0.4% respectively. These are significantly lower than what is typically seen for Seyfert 1 galaxies (ratios between 2% and 15%, Elvis et al. 1994) and are consistent with both sources being extremely under-luminous in X-ray emission, similar to that seen in other ULIRGs (Teng et al. 2015), which has been attributed to higher Eddington ratios. Future hard X-ray observations of the two sources at energies $> 10 \text{ keV}$ are needed to confirm this hypothesis. Meanwhile, we treat the L_{AGN} from X-ray observations as lower limits on the AGN luminosity.

4.2.4. Other AGN diagnostics

We also mention other commonly used optical/near-IR/mid-IR AGN diagnostics for completeness. These in-

clude high-ionization mid-IR lines - e.g. [Ne V] $14.3 \mu\text{m}$ and [Ne VI] $7.6 \mu\text{m}$ - which are only detected in AGN-host sources, and the optical lines [O III]/ $\text{H}\beta$, whose ratio is used to characterize line ionization and the hardness of the radiation field.

Neither IRAS 20100–4156 or IRAS 03158+4227 display the high-ionization lines which are most commonly seen in AGN host galaxies, though they display the lower-energy [Ne II] and [Ne III] lines (Farrah et al. 2007). The ratio of the two probes the hardness of the radiation field, with starburst dominated galaxies showing a line ratio of $-1.3 \lesssim \log([\text{NeIII}]/[\text{NeII}]) \lesssim 0.1$ in a sample of GOALS galaxies, though highly starbursting galaxies can show high ratios up to $\log([\text{NeIII}]/[\text{NeII}]) > -0.2$; Inami et al. 2013). We find $\log([\text{Ne III}]/[\text{Ne II}]) \sim -0.4$ and ~ -0.8 for IRAS 20100–4156 and IRAS 03158+4227, respectively, which are consistent with the starburst range. Similarly, IRAS 20100–4156 and IRAS 03158+4227 show [O III]/ $\text{H}\beta \sim 1.2$ and [O III]/ $\text{H}\beta \sim 2.3$, respectively (Staveley-Smith et al. 1992; Meusinger et al. 2001), which are too low for AGN, but are consistent with LINER ratios based on the BPT diagnostic diagram (Kewley et al. 2006). Near-IR spectroscopy of the Pa- α and Br γ lines for IRAS 20100–4156 also does not show broad pedestals in the spectral lines which would be evidence for emission from a broad line region (BLR).

Overall, these diagnostics are consistent with the significant dust-obscuration observed in the two sources, and we therefore cannot comment on the AGN luminosity based on any of these.

4.2.5. Uncertainties in AGN fraction

IRAS 20100–4156 and IRAS 03158+4227 are extremely dust-obscured sources, with high silicate optical depths (Spoon et al. 2013), and high nuclear column densities, as evidenced by the deep absorption in far-IR OH lines (González-Alfonso et al. 2017). This extreme obscuration renders most line diagnostics ineffective. This high dust-obscuration also impacts the mid-IR decomposition, which is no longer applicable if the hot dust emission is completely obscured by cooler surrounding dust, as the warmer photons will be re-emitted at longer wavelengths. Another caveat for mid-IR decomposition is that the starburst template used for decomposition is derived using a combination of mid-IR spectra from starburst-dominated ULIRGs, which could always include some small AGN component in principle, possibly biasing the method towards finding higher starburst fractions. We note, however, that IRAS 08572+3915, an AGN-dominated highly obscured ULIRG (Efstathiou et al. 2014), is correctly identified as a highly AGN-

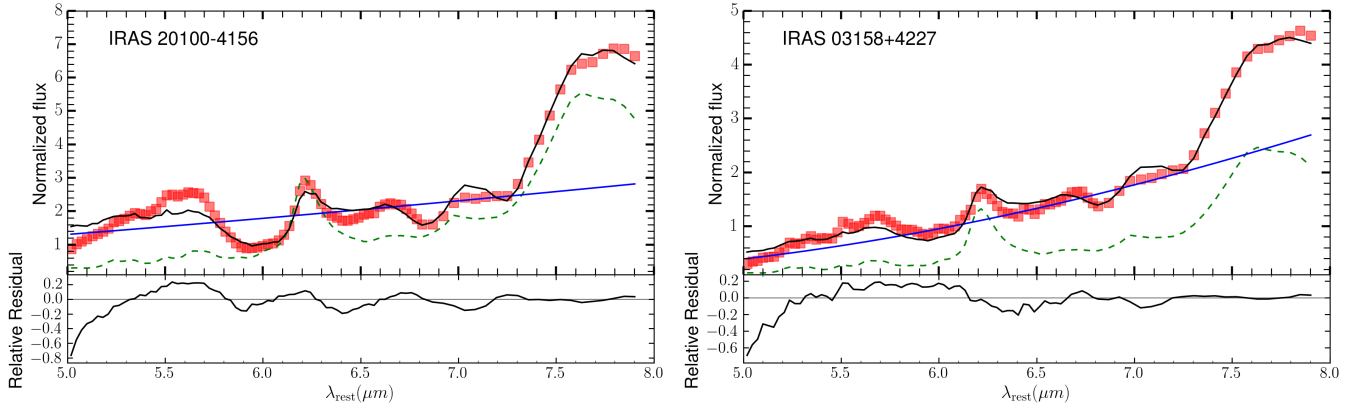


Figure 10. Results of mid-IR spectral decomposition in IRAS 20100–4156 and IRAS 03158+4227. The dashed green line shows a starburst template, the red points show the observed IRS spectrum, and the blue line shows the AGN continuum emission, while the black line shows the weighted sum of the two components after incorporating water-ice features. The lower panels in each show the relative residuals at each point.

dominated galaxy based on mid-IR decomposition, despite showing a deeper silicate optical depth (also no [Ne V] emission), and a geometry consistent with an edge on torus, similar to the geometry for IRAS 20100–4156 and IRAS 03158+4227. This strongly suggests that a significant fraction of mid-IR photons can escape through optically thin lines of sight, despite high dust opacities. This scenario has been supported by simulations (e.g. Roth et al. 2012; Novak et al. 2012; Krumholz & Thompson 2013; Skinner & Ostriker 2015), although the results are sensitive to the numerical methods in question (Davis et al. 2014; Tsang & Milosavljević 2015). Overall, we do not find any evidence that the mid-IR decomposition is finding artificially low AGN fractions for our targets, though we cannot rule out more luminous and deeply buried AGN with their dust torus completely obscured by cooler molecular gas.

5. DISCUSSION

Here we discuss the outflows in IRAS 20100–4156 and IRAS 03158+4227 in the context of other known molecular outflows. We compile all published observations of molecular gas outflows using CO(1–0) in the local universe (Table 4). We restrict this sample to ULIRGs, as feedback in lower-mass galaxies ($M_* \sim 10^{10} - 10^{11} M_\odot$) often occurs in ‘radio’ mode via relativistic jets. Such outflows have much smaller mass outflow rates ($\dot{M} \lesssim 50 M_\odot \text{ yr}^{-1}$) and may quench star formation by injecting turbulence and decreasing the star formation efficiency (e.g. Alatalo et al. 2015) rather than sweeping out the molecular gas and dust at high rates. Given the physically distinct feedback mechanism in these systems, we do not include them in our analysis. Furthermore, the method of mid-IR decomposition has been calibrated for use in ULIRGs (Nardini et al. 2010; Nar-

dini & Risaliti 2011). Most of the ULIRGs in our sample also show signatures of outflowing molecular gas in *Herschel* far-IR OH spectra (see Table 4 and references within), and are thus drawn from a similar parent sample as IRAS 20100–4156 and IRAS 03158+4227. Since more IR-luminous galaxies typically become more AGN-dominated, including sources with IR luminosities varying over 2 orders of magnitudes can potentially introduce a bias towards finding a correlation between outflow properties and AGN luminosities. This is avoided by selecting galaxies at comparable IR luminosities.

We determine the outflow energy flux and momentum for this sample of ULIRGs as described in § 4.1. We determine the AGN fraction f_{AGN} for these sources using mid-IR decomposition, as described in § 4.2, and calculate the IR luminosity as described in Sanders & Mirabel (1996). This ensures that IR luminosities are compared consistently between our targets and the rest of the ULIRG sample. The AGN and nuclear starburst luminosities are defined as $L_{\text{AGN}} \sim f_{\text{AGN}} L_{\text{IR}}$ and $L_* \sim (1 - f_{\text{AGN}}) L_{\text{IR}}$, respectively. Together with IRAS 20100–4156 and IRAS 03158+4227, we also highlight outflow properties for IRAS 08572+3915 and Mrk 231, which host comparably powerful outflows, while featuring dust obscuration properties (based on the silicate optical depth $\tau_{9.7\mu\text{m}}$ as defined by Spoon et al. 2007) which bracket the two sources of interest, IRAS 03158+4227 and IRAS 20100–4156.

5.1. Outflow energetics

Galaxy-wide molecular outflows can be driven by AGN, nuclear starbursts, or a combination thereof, all of which will result in different outflow energy and momentum fluxes. AGN-driven outflows can have two phases: an energy-conserving phase, where the hot shocked bub-

Table 3. Properties of outflow wings (see § 3.1.2, § 3.2.2 for details)

Source	Core		red wing		blue wing		size
	S_{CO} (Jy km s ⁻¹)	Velocity range (km s ⁻¹)	S_{CO} (Jy km s ⁻¹)	Velocity range (km s ⁻¹)	S_{CO} (Jy km s ⁻¹)	R (kpc)	
IRAS 20100–4156	(11.2 ± 0.3)	(440,1650)	(0.54 ± 0.03)	(-1169, -466)	(0.58 ± 0.03)	1.0 ± 0.2	
IRAS 03158+4227	(8.4 ± 0.7)	(400,1750)	(0.80 ± 0.22)	(-944, -413)	(0.31 ± 0.15)	1.9 ± 1.3	

Table 4. All properties of outflow sources.

Name	z	M_{gas}^a (M_{\odot})	$\log_{10}(L_{\text{IR}})^b$ (L_{\odot})	f_{AGN}^c	L_{AGN}^d (ergs s ⁻¹)	\dot{M}_{OF} (M_{\odot} yr ⁻¹)	$v_{\text{OF}}^{\text{AVG}}$ (km s ⁻¹)	$\log_{10}(\tau_{\text{dep}})$ (yrs)	$\dot{P}_{\text{OF}}/(L_{\text{AGN}}/c)$	$\log_{10}(\dot{E}_{\text{OF}})$ (ergs s ⁻¹)	Ref
IRAS 20100–4156	0.129	9.85	12.63	0.14	45.35	672	929	7.04	53	44.26	(1)
IRAS 03158+4227	0.134	9.75	12.6	0.43	45.82	350	876	7.11	9	43.93	(1)
Mrk 231	0.042	9.73	12.49	0.42	45.70	352	700	7.19	9	43.73	(2)
IRAS 08572+3915	0.058	9.18	12.10	0.91	45.64	406	800	6.57	14	43.91	(3)
IRAS F10565+24489	0.043	9.90	12.00	0.05	44.28	98	450	7.91	43	42.79	(3)
IRAS 23365+3604	0.064	9.93	12.17	0.05	44.46	55	450	8.19	16	42.54	(3)
Mrk 273	0.038	9.70	12.13	0.07	44.56	200	620	7.40	65	43.38	(3)
IRAS 17208–0014 ^e	0.042	9.50	12.38	0.05	43.97	163	400	7.29	131	42.91	(4)
IRAS 11119+3257 ^e	0.190	9.95	12.65	0.48	45.91	153	600	7.67	2	43.18	(5)

^aCalculated assuming an $\alpha_{\text{CO}} = 0.8 M_{\odot} (\text{K km s}^{-1} \text{ pc}^{-2})^{-1}$.

^bCalculated using the prescription from Sanders & Mirabel (1996)

^cCalculated using mid-IR decomposition

^d $L_{\text{AGN}} = f_{\text{AGN}} L_{\text{IR}}$.

^eFor these two ULIRGs we have estimated the average outflow velocity using visual inspection of the published spectra.

References—(1) This work (2) Cicone et al. (2012) (3) Cicone et al. 2014 (4) García-Burillo et al. (2015) (5) Veilleux et al. (2017)

Table 5. SED-FITTING RESULTS AND OTHER PHYSICAL PARAMETERS (§ 4.2.1)

Source	z	f_{AGN}	L_{dust} ($10^{11} L_{\odot}$)	U_{min}	M_{dust} ($10^8 M_{\odot}$)	M_{gas} ($10^9 M_{\odot}$)	M_{*} ($10^{11} M_{\odot}$)	SFR ($M_{\odot} \text{ yr}^{-1}$)	sSFR (Gyr ⁻¹)	δ_{GDR}
IRAS 20100–4156	0.129	0.2 ± 0.1	2.9 ± 0.2	35	4.2 ± 0.2	7.8	5.5 ± 0.3	198 ± 10	3.2	16
IRAS 03158+4227	0.134	0.3 ± 0.1	2.9 ± 0.2	29	5.0 ± 0.5	6.4	18.6 ± 0.9	244 ± 12	1.4	13

NOTE—The gas masses were calculated using $\alpha_{\text{CO}} = 0.8 M_{\odot} (\text{K km s}^{-1} \text{ pc}^2)^{-1}$, based on CO($J = 1 \rightarrow 0$) observations.

ble expands on timescales significantly shorter than its radiative cooling timescale and outflow energy is conserved, or a momentum-conserving phase, wherein the expansion and cooling timescales are comparable and the momentum is conserved (e.g. Zubovas & King 2012). Energy conserving outflows are created when AGN-driven energetic nuclear winds ($v_{\text{in}} \sim 0.1 - 0.3c$) collide with the ISM, resulting in shocked hot gas which cools inefficiently. The resulting outflow is nearly adiabatic and can produce significant momentum boosts⁶ $\dot{P} \sim \beta(L_{\text{AGN}}/c)v_{\text{in}}/v_{\text{OF}} \sim 10L_{\text{AGN}}/c$ for $\beta \sim 0.5$, $v_{\text{in}} \sim 0.1c$ and $v_{\text{OF}} \sim 1500 \text{ km s}^{-1}$, where β is the fraction of the energy converted to bulk motion of the ISM (derived to be $\beta \sim 0.5$ for an expanding adiabatic bubble, while the rest of the energy goes into the thermal pressure of the shocked bubble; Weaver et al. 1977; Faucher-Giguère & Quataert 2012). This model is observationally supported by detections of high momentum boosts in molecular gas outflows, which imply that nearly all outflows in ULIRGs pass through at least a partially energy-conserving phase, during which the momentum boost is imprinted (González-Alfonso et al. 2017). Furthermore, relativistic ionized nuclear winds which drive the outflows have been detected using X-ray spectroscopy (Tombesi et al. 2015; Feruglio et al. 2015; Nardini et al. 2015), and energy has been shown to be conserved between the relativistic and molecular phases of the outflow (Feruglio et al. 2015; Veilleux et al. 2017). Theoretically, the mechanical luminosity imparted to the nuclear wind is $\dot{E} \sim \dot{M}_{\text{in}}v_{\text{in}}^2/2 \sim (L_{\text{AGN}}/c)v_{\text{in}}/2 \sim 5\%L_{\text{AGN}}$ for $v_{\text{in}} \sim 0.1c$ (see King & Pounds 2015, for a derivation). Of this, $\sim 20\% - 50\%$ can be translated into bulk motion of the shocked ISM layer (Faucher-Giguère & Quataert 2012; Richings & Faucher-Giguère 2017b).

On the other hand, feedback from nuclear starburst activity takes place via supernovae, stellar winds, and HII regions, and is expected to produce more modest momentum boosts; for example, a 40 Myr old starburst produces a momentum boost of $\dot{P} \sim 3.5L_*/c$ (Leitherer et al. 1999; Veilleux et al. 2005). This expression includes both the momentum deposition by SNe and stellar winds at a level $\sim 2.5L_*/c$, and a radiation pressure term L_*/c under the assumption of a single photon scattering event. In the case of radiation pressure on optically thick dust (column densities $\geq 10^{23} \text{ cm}^{-2}$), multiple photon scatterings can lead to a higher momentum boost, $\dot{P} \sim \tau_{\text{IR}}(L/c)$, where L is either the AGN or the starburst luminosity (Thompson et al. 2015). However, this cannot lead to arbitrarily high momentum boosts

even in nuclei with large IR optical depths, and the momentum boost is limited to $\dot{P} \lesssim 5L_{\text{IR}}/c$, as radiative transfer models for dusty nuclei find that photons can escape through optically thin lines of sight despite high dust opacities (e.g. Roth et al. 2012; Novak et al. 2012; Krumholz & Thompson 2013; Skinner & Ostriker 2015), although the results are sensitive to the numerical methods in question (Davis et al. 2014; Tsang & Milosavljević 2015). The maximum mechanical energy that can be transferred to the outflow for a 40 Myr old starburst is $\dot{E} = 7 \times 10^{41} \text{ SFR}/(M_{\odot} \text{ yr}^{-1}) \text{ ergs s}^{-1}$, which is equivalent to $\dot{E} \sim 1.8\%L_*$, of which $\sim 25\%$ can be efficiently transferred to bulk motion of the gas. Comparing observed outflow energy and momenta (Table 4) to different theoretical predictions therefore allows us to constrain the outflow driving mechanism.

5.1.1. Momentum

Here we compare the inferred outflow momentum fluxes (\dot{P}_{OF}) to the expected momentum injection due to starburst and/or AGN activity i.e. L_{AGN}/c , L_*/c , L_{IR}/c , and the predicted momentum injected from the sum of both (to first order, $\dot{P}_{\text{sum}} \sim 20L_{\text{AGN}}/c + 3.5L_*/c$) for our sample of ULIRGs (Fig. 11).

We find that starburst activity alone is sufficient to provide the observed momentum boosts only in the weakest three outflows. We also find that nearly all the outflows show significant momentum boosts relative to the L_{AGN} , $\dot{P}_{\text{OF}} \sim (5 - 50)L_{\text{AGN}}/c$. While these results are consistent with previous molecular gas outflow observations (e.g. Ciccone et al. 2014; González-Alfonso et al. 2017), we also find significant differences. We find that high momentum boosts up to $\dot{P}_{\text{OF}} \sim 10L_{\text{IR}}/c$ are not restricted to ULIRGs with $f_{\text{AGN}} \gtrsim 0.5$, but are seen in ULIRGs with a range of $f_{\text{AGN}} \sim 0.2 - 0.9$. We detect no significant correlation between the outflow momentum flux and L_*/c and L_{IR}/c (Spearman correlation coefficient $r(\dot{P}_{\text{OF}}, L_{\text{IR}}/c) \sim r(\dot{P}_{\text{OF}}, L_*/c) \sim 0.3$; p-value ~ 0.5). We find a similar lack of correlation between the inferred outflow momentum flux and L_{AGN}/c (Spearman correlation coefficient $r(\dot{P}_{\text{OF}}, L_{\text{IR}}/c) \sim 0.4$; p-value ~ 0.3) and \dot{P}_{sum} (Spearman correlation coefficient $r(\dot{P}_{\text{OF}}, \dot{P}_{\text{sum}}) \sim 0.4$; p-value ~ 0.4)⁷.⁸

⁷ The Spearman coefficient measures the monotonicity of the correlation between two quantities, while a Pearson correlation measures the linearity of the correlation between two. We did not recover significant correlations using either diagnostic.

⁸ IRAS 08572+3915 is the only AGN-dominated ULIRG with a relatively low total L_{IR} . However, it has been suggested that due to the extreme dust obscuration, and the torus axis being perpendicular to the line of sight, its IR luminosity could be underestimated by as much as a factor of 5 (Efsthathiou et al. 2014).

⁶ see González-Alfonso et al. 2017, section 7.2 for a derivation

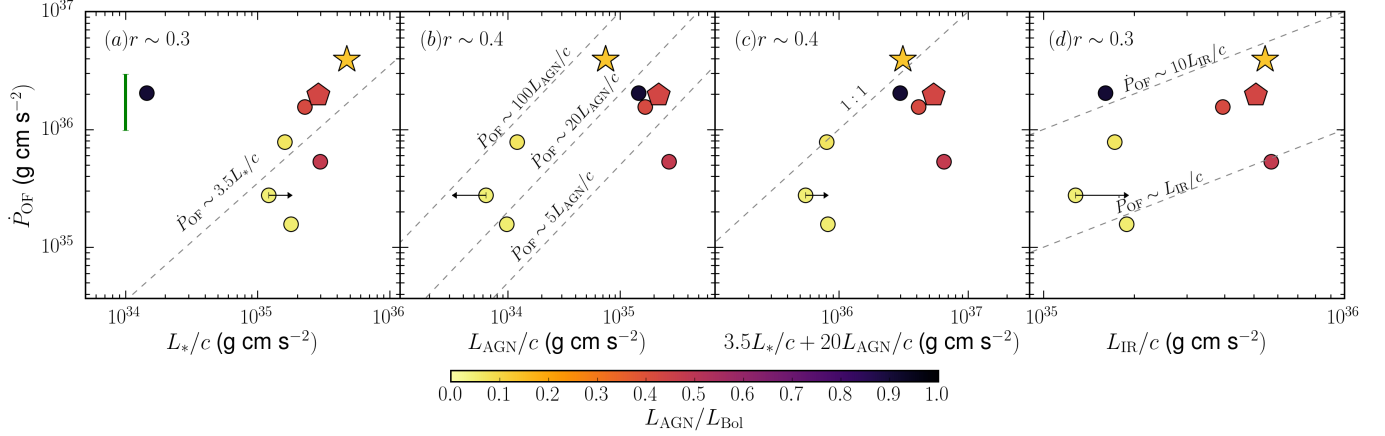


Figure 11. Inferred outflow momentum flux (\dot{P}_{OF}) as compared to (a) L_*/c (b) L_{AGN}/c (c) the predicted sum of the AGN and starburst momentum fluxes, \dot{P}_{sum} , and (d) L_{IR}/c . The star and pentagon show IRAS 20100–4156 and IRAS 03158+4227, respectively, while filled circles represent other ULIRGs for which molecular outflows have been observed in CO. Dashed lines show the expected coupling fraction between the momentum fluxes from AGN/starburst and the outflow momentum flux. The color of the points represents the f_{AGN} , with darker points being more AGN-dominated galaxies. The green bar shows the representative uncertainty in the outflow momentum flux.

The observed momentum boost for IRAS 03158+4227 ($\dot{P} \sim 9L_{\text{AGN}}/c$) is consistent with the boosts predicted for AGN-driven outflows. For IRAS 20100–4156, on the other hand, we observe a high momentum boost ($\dot{P} \sim 53L_{\text{AGN}}/c$). The momentum boost is higher than expected in starburst-dominated outflow sources ($\dot{P} \sim 10L_*/c$ for IRAS 20100–4156, while $\dot{P} \sim 2-4 \times L_*/c$ for starburst galaxies, [Leitherer et al. 1999](#); [Veilleux et al. 2005](#)). Such high momentum boosts can in principle be generated in deeply dust-obscured starburst nuclei ($\tau_{\text{IR}} \gg 1$) with high surface densities of star formation (Σ_{SFR}), such that the star formation is Eddington-limited by radiation pressure on dust ($\Sigma_{\text{SFR}} \sim 3000M_{\odot} \text{ yr}^{-1} \text{ kpc}^{-2}$, [Murray et al. 2005](#); [Thompson et al. 2005](#)). However, [Roth et al. \(2012\)](#) find that in such optically thick nuclei photons preferentially escape along optically thin lines-of-sight and limit the momentum boost to $\sim 5L_{\text{IR}}/c$. Furthermore, the high maximum outflow velocity in IRAS 20100–4156 is also unusual for starburst driven outflows, although not impossible. Previous studies have consistently found significant correlations between the maximum outflow velocities in molecular gas outflows and L_{AGN} ([Sturm et al. 2011](#); [Spoon et al. 2013](#); [Veilleux et al. 2013](#); [Stone et al. 2016](#)), suggesting that AGN are responsible for the fastest-moving components of the outflow. Compact, Eddington-limited starburst activity has also been suggested to drive the high-velocity molecular outflow ($\sim 1000 \text{ km s}^{-1}$) in a $z \sim 0.7$ galaxy ([Geach et al. 2014](#)), although the host

galaxy is much less massive. While observations of outflows in starburst galaxies show that their maximum outflow velocities are strongly correlated with Σ_{SFR} , these probe ionized gas outflows, and the star formation surface densities are far below the Eddington limit ([Heckman et al. 2015](#); [Heckman & Borthakur 2016](#)). For IRAS 20100–4156, assuming a radius of $\lesssim 0.2 \text{ kpc}$ for the nuclear starburst and calculating the nuclear SFR $\sim 10^{-10}(L_*/L_{\odot})(M_{\odot} \text{ yr}^{-1})$, we find a surface density of star formation $\Sigma_{\text{SFR}} \gtrsim 3000M_{\odot} \text{ yr}^{-1} \text{ kpc}^{-2}$, which is above the Eddington limit. Overall, the outflow in IRAS 20100–4156 could in principle be driven purely by the starburst.

However, we consider this scenario unlikely based on the high outflow velocity observed. We instead favor the scenario that the outflow in IRAS 20100–4156 is driven by a combination of AGN and starburst activity, as neither AGN or the starburst feedback alone can provide the observed momentum boost, which we reiterate is a conservative estimate.

5.1.2. Energy

We compare the outflow energy flux (\dot{E}_{OF}) for all ULIRGs in our sample to L_{AGN} , L_* , L_{IR} , and the predicted energy flux from a combination of AGN and starburst activity ($\dot{E}_{\text{sum}} = 0.05L_{\text{AGN}} + 0.02L_*$, [Fig. 12](#)). We find that starburst activity can power the most massive outflows only if all the mechanical luminosity from supernovae and stellar winds is converted into bulk motion of the gas with 100% efficiency, which is unrealistic. However, weaker outflows can be powered by stellar feedback even when realistic efficiencies are taken into account. Similarly, the outflows can

Correcting for this factor would marginally improve the correlations described above.

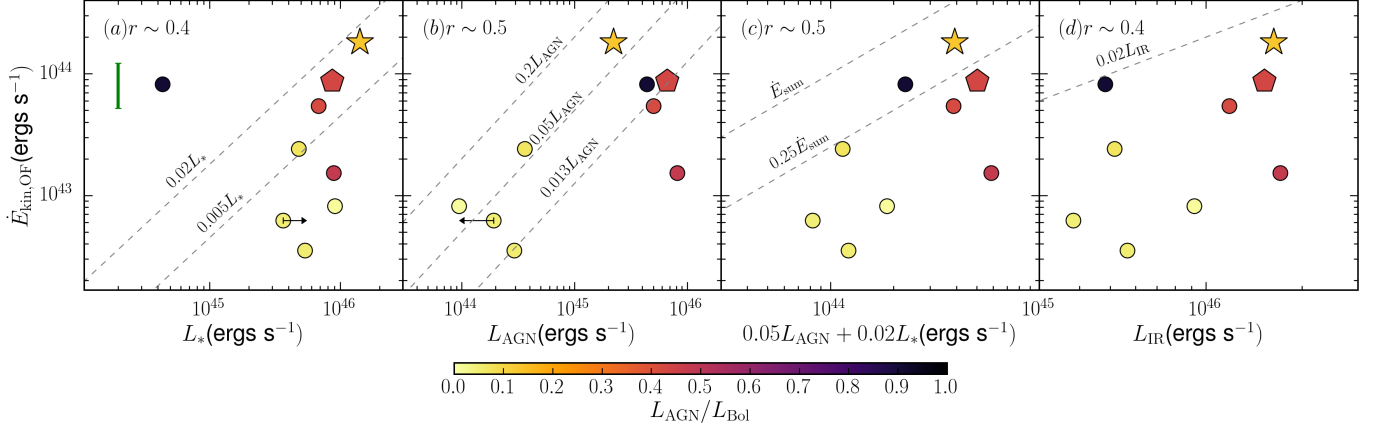


Figure 12. Inferred outflow kinetic energy flux ($\dot{E}_{\text{kin,OF}}$) compared to (a) L_* (b) L_{AGN} , (c) the predicted sum of AGN and starburst energies \dot{E}_{sum} , and (d) L_{IR} respectively for the ULIRG sample. The conventions are the same as in Fig. 11, and the dashed lines show the expected coupling fraction between AGN/starburst luminosities and the outflow kinetic energy flux. IRAS 20100–4156 would need to have an unrealistic coupling efficiency of $\gtrsim 8\%$ with the AGN luminosity, suggesting that both AGN and starburst activity need to play a role in driving the outflow in IRAS 20100–4156. The green errorbar shows the representative uncertainty in the outflow energy fluxes for the sample.

be powered purely by AGN (i.e show energy fluxes $\sim 1 - 3\%L_{\text{AGN}}$) only in ULIRGs with $f_{\text{AGN}} \gtrsim 0.4$, but not in starburst dominated galaxies. We do not find that the outflow energy fluxes increase significantly with L_{AGN} and with \dot{E}_{sum} (Spearman correlation coefficients $r(\dot{E}_{\text{OF}}, L_{\text{AGN}}) \sim 0.5$, $r(\dot{E}_{\text{OF}}, \dot{E}_{\text{sum}}) \sim 0.5$; p-values ~ 0.3 and ~ 0.2 , respectively). We find a similar lack of correlation with L_* and L_{IR} (Spearman correlation coefficients $r(\dot{E}_{\text{OF}}, L_*) \sim 0.4$, $r(\dot{E}_{\text{OF}}, L_{\text{IR}}) \sim 0.4$; p-value ~ 0.4 for both). We find that powerful outflows are detected in ULIRGs with f_{AGN} with a wide range of $\sim 0.2 - 0.9$.

We find that IRAS 03158+4227 shows an outflow energy flux of $\sim 1\%L_{\text{AGN}}$, which is close to the expected scaling. The outflow in IRAS 20100–4156, however, shows an outflow energy flux of $\sim 8\%L_{\text{AGN}}$, which is significantly higher than predicted from AGN activity alone. We therefore conclude that it is driven by a combination of the two, which is consistent with findings in the previous section.

5.2. What drives the most powerful outflows?

We have compared the outflow energy and momentum fluxes in IRAS 20100–4156 and IRAS 03158+4227 against theoretical predictions and outflows in other ULIRGs, drawn from the same parent ULIRG sample and with similar observations of CO(1–0). Despite the relatively small range in L_{IR} , our sample demonstrates a range in \dot{P}_{OF} and $\dot{E}_{\text{OF,kin}}$ varying over two orders of magnitude, and can therefore be used to test for correlations with the AGN and starburst luminosities. For the complete sample, we find no significant correlation between the molecular outflow properties and L_{AGN} , L_* , or

a combination of the two. We also find that the strongest outflows span a large range in $f_{\text{AGN}} = 0.2 - 0.9$, despite having very similar IR luminosities i.e. f_{AGN} is a poor proxy for the strength of feedback (also see Farrah et al. 2012). We also find that starburst activity can play an important role even in the most massive outflows, as demonstrated by IRAS 20100–4156. The lack of dependence of outflow properties on f_{AGN} suggests that previously seen correlations between outflow properties and AGN luminosities may be partly driven by the bias that ULIRGs statistically show higher f_{AGN} at higher IR luminosities (Nardini et al. 2010; Alonso-Herrero et al. 2012; Alonso-Herrero 2013), as compared to smaller galaxies.

5.3. OHM as a possible new tracer for outflows

We report the first detection of OHM emission from IRAS 03158+4227 (Fig. 6) and a detection of time-variable OHM emission from IRAS 20100–4156, including significant emission from its high-velocity outflow wings (Fig. 2, Fig. 13). The OHM emission in IRAS 20100–4156 was first reported by Staveley-Smith et al. (1989), although they could not confirm the high-velocity outflow wings due to limited bandwidth and non-linearities in the spectral baseline in their single-dish observations. More recent observations of IRAS 20100–4156 were conducted independently in 2015 using the Australia Compact Array (ATCA) and Australian Square Kilometre Array Pathfinder (ASKAP)’s Boolardy Engineering Test Array (BETA), where high-velocity wings were also detected, although with a lower significance (Harvey-Smith et al. 2016). These authors interpreted the high-velocity components as maser emis-

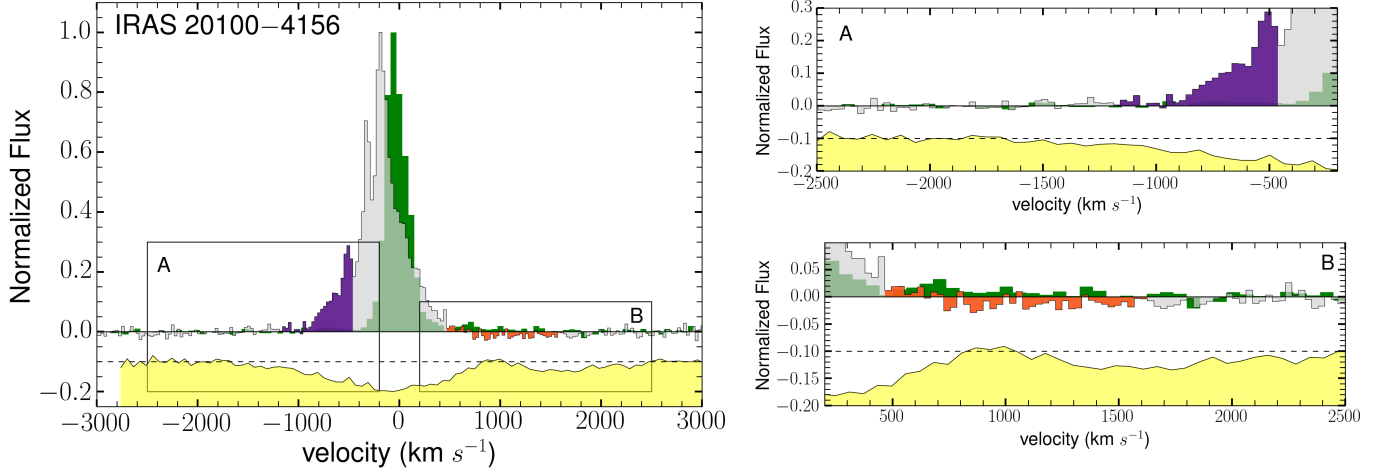


Figure 13. Overlaid spectra for CO(1 – 0) emission (green), OH 119 μm P-Cygni line profile (yellow, normalized to a zero of -0.1), and OH 1.667 GHz emission (grey) from IRAS 20100–4156. The purple and orange regions show the red and blue outflow wings respectively. The A and B panels show the zoomed in regions around the red and blue outflow wings. We detect only the blue outflow wing in OHM emission, while the red wing shows tentative evidence for absorption.

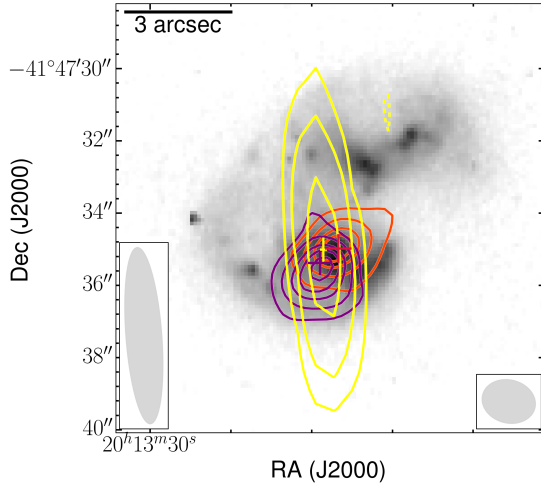


Figure 14. Spatial extent of the OHM emission as compared to the red and blue outflow wings seen in CO(1 – 0) in IRAS 20100–4156. Emission is shown as $\pm 4, 5, 6\sigma$ significance contours for the outflow wings, and $\pm 10, 20, 30, 40\sigma$ contours for OHM emission. Colored crosses show the peak pixel and their lengths represent the 3σ positional uncertainty for each of OHM (yellow), red, and blue outflow wings. The OHM emission is nearly co-spatial with the blueshifted outflow wing, which is consistent with enhanced OHM emission detected from the blueshifted outflowing molecular gas.

sion from molecular gas clumps rotating about a central SMBH ($M_{\text{BH}} \sim 2.8 \times 10^9 M_{\odot}$, radius $r \sim 50$ pc), with the narrow-line components potentially associated with double nuclei, or with an outflow.

Our observed OHM spectrum for IRAS 20100–4156 is consistent with the published ASKAP/BETA spectra, and has significantly better sensitivity. The OHM emission from IRAS 20100–4156 can be decomposed into a

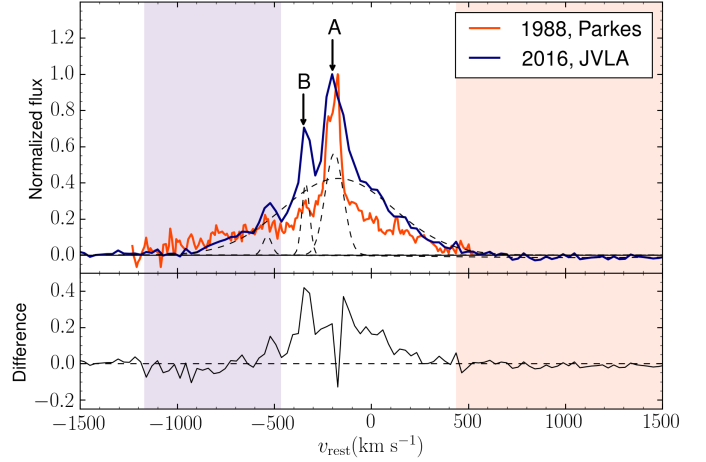


Figure 15. OHM spectra from IRAS 20100–4156 observed at different epochs, from 1988 to 2016. The spectrum from [Staveley-Smith et al. \(1989\)](#) has not been continuum subtracted, due to the lack of an extended baseline i.e the normalization of the two spectra are uncertain. We here normalize to the same peak, to highlight changes in the spectral line profiles. The line profiles clearly show the presence of a varying narrow line component at ~ -350 km s^{-1} , and possibly one at ~ -550 km s^{-1} . These suggest the presence of compact masing sources with sizes of ~ 10 pc, which would be consistent with previous VLBI observations of OH megamasers.

broad component, together with multiple narrow components (Fig. 13). It shows a strikingly different velocity profile as compared to the CO(1 – 0), with a systemic blueshift in the line core, enhanced emission from the blueshifted outflow wing, and tentative evidence of redshifted absorption in the OHM line profile (Fig. 13). Despite these differences, the velocity extent of the de-

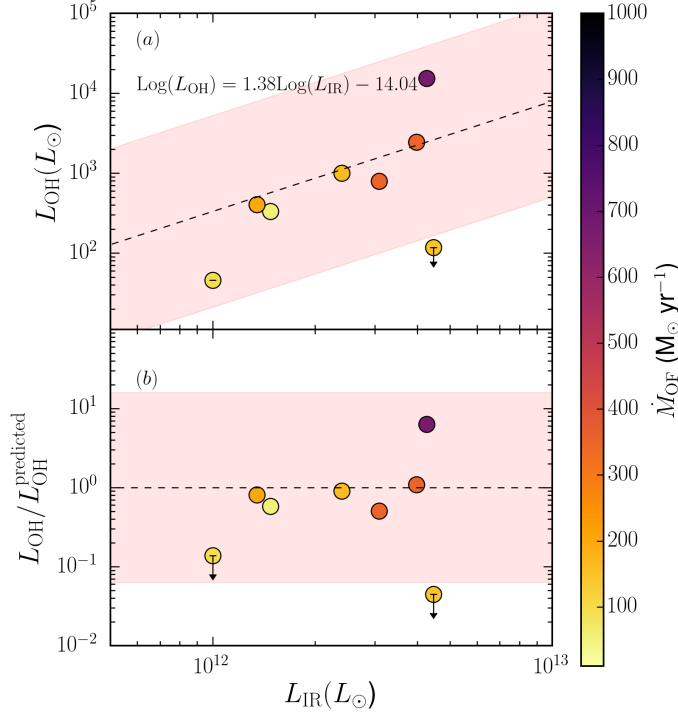


Figure 16. (a) The OHM luminosity as a function of the IR luminosity L_{IR} . The $L_{\text{OH}} - L_{\text{IR}}$ correlation from Yu (2003) is shown as the black dashed line, and the shaded pink region shows the ± 1.2 dex spread around the best-fit relation. All outflow sources that have been observed in OHM emission have been shown, compiled from Yu (2003); Willett et al. (2011) (b) L_{OH} , normalized by the predicted $L_{\text{OH}}^{\text{predicted}}$ from the $L_{\text{IR}} - L_{\text{OH}}$ relation. The color of the points represents the CO-inferred mass outflow rate \dot{M}_{OF} . ULIRGs with higher mass outflow rates \dot{M}_{OF} have higher L_{OH} .

tected wings agrees remarkably well with previous detections of the outflowing molecular gas - CO(1–0) and OH 119 μm . This is excluding the velocity offset between the CO and OHM peak emission, which is not surprising given the extremely compact nature of OHM emission (e.g. $\lesssim 0.2$ kpc; Pihlström et al. 2005). The peak of the OHM emission could also be tracing the low-velocity outflow ($v_{\text{outflow}} \sim 200$ km s $^{-1}$), which would be in line with the systematic blueshift of OH 65 μm absorption detected in ULIRGs (González-Alfonso et al. 2017).

We detect a spatial offset of $\sim 0.9 \pm 0.3$ kpc between the OHM emission (spatially unresolved) and the peak of the CO(1–0) emission in IRAS 20100–4156, indicating a non-circumnuclear origin for the maser emission unlike previous OHM maps (e.g. Pihlström et al. 2001; Klöckner et al. 2003; Rovilos et al. 2003), as shown in Fig. 14. The OHM emission is co-spatial with the blue outflow wing as detected in CO, and at a small offset from the peak of the red outflow wing emission. While

numerous previous observations have reported asymmetries in OHM emission, potentially due to outflows (e.g. Baan et al. 1989, 1992), this is the first direct comparison between spatially resolved powerful molecular outflows detected in CO and OHM that we are aware of.

Spatially resolved OHM observations have revealed that the emission comprises two components: compact, high-gain saturated OHM emission on $\sim 1 - 10$ pc scales, and low-gain unsaturated diffuse emission over larger scales (~ 100 pc; e.g. Lonsdale et al. 1998, 2003). The observed OHM spectrum for IRAS 20100–4156 is consistent with this picture if the broad pedestal traces the large-scale diffuse emission, and the narrow features traces dense embedded clumps of OHM emission. OHM emission is also predominantly from warm, dense molecular gas with $n_{\text{H}_2} \sim 10^4$ cm $^{-3}$ and gas/dust temperatures of $\gtrsim 100$ K, allowing us to put the first constraints on the gas density and temperature in the outflowing molecular gas in IRAS 20100–4156. Such physical conditions, favorable for OH masing, are also associated with intense star formation activity (see Lo 2005, for a review), which is also reflected in the strong correlation between the occurrence of OHM emission and high dense molecular gas fractions (which trace actively star-forming molecular gas, Gao & Solomon 2004a,b), traced by HCN (Darling 2007; Willett et al. 2011). It is therefore interesting to explore whether the excess emission in the outflow wings is tracing ongoing star formation in outflowing molecular gas (e.g. Maiolino et al. 2017). One of the more puzzling aspects of the OHM emission is the marked asymmetry between the red and blue outflow wing emission. In the velocity range of the red outflow wing, we instead tentatively detect redshifted absorption (Fig. 13, B), which implies the presence of continuum emission behind the redshifted outflowing gas along the line of sight. One explanation is that this continuum emission is synchrotron emission, either from relativistic electrons generated by the forward shock associated with the molecular outflow (see González-Alfonso et al. 2018), or due to a localized starburst where the outflow interacts with the galaxy-wide ISM. This continuum emission can then act as the background for the OH 1.667 GHz redshifted absorption relative to the observer. If this scenario is correct, the detection of OH 1.667 GHz emission/absorption from outflowing gas in other ULIRGs will depend sensitively on the outflow opening angle and the relative orientation of the outflow axis to our line-of-sight. Alternatively, it is possible that there is a compact secondary AGN nucleus in IRAS 20100–4156 along the line of sight, and the receding outflow component is seen in OHM absorption against the continuum emission from this nucleus (e.g. Ballo et al.

2004). In order to differentiate between these hypotheses, observations with much higher spatial resolution are required.

The multi-epoch observations of OHM emission from IRAS 20100–4156 also allow for identification of time-variable components, which in turn constrain the size-scales of the emission. In Fig. 15, we compare the normalized emission from Staveley-Smith et al. (1989) to our observations. Given the limited bandwidth of the Parkes observations which do not cover any non-line continuum, we do not perform continuum subtraction and assume that the peak of the spectral line remains constant. This allows us to identify any relative changes in the line profile. We find a significant excess in OHM emission in 2016 as compared to 1988, with the largest change in component B (see Fig. 15), and with a smaller increase between -500 km s^{-1} to 500 km s^{-1} . This observed increase in emission from component B is consistent with that detected in Harvey-Smith et al. (2016). The time-variation in OHM emission from the narrow line region implies an origin of a length scale $\lesssim 10 \text{ pc}$, which is consistent with compact luminous masing clumps.

We also test whether OHM emission is preferentially enhanced in molecular outflow hosts by compiling previous OHM observations for our sample of powerful molecular outflow sources (Fig. 16). We compare them to the previously determined $L_{\text{OH}} - L_{\text{IR}}$ correlation (Darling & Giovannelli 2002a,b). We find that stronger molecular outflows appear to be preferentially detected in sources with increased OHM luminosity, after controlling for the correlation with the IR luminosity. Outflow observations using OHM emission are also observationally cheaper than CO - the peak-to-line wing ratio in IRAS 20100–4156 is ~ 7 times higher than that for CO(1–0). This translates to a relative reduction by a factor of ~ 50 in observing time between CO and OHM emission. All of these suggest that OHM activity is an exciting avenue in which to explore the properties of molecular outflows in a much larger sample of galaxies, and at higher redshifts (up to $z \sim 0.7$ with the VLA).

6. CONCLUSIONS AND FUTURE WORK

We have presented spatially resolved molecular gas observations of the two most powerful outflows in the local universe, and placed them in the context of other known molecular outflows in ULIRGs drawn from the same parent sample.

- Our observations reveal extremely fast ($v_{\text{max}} \gtrsim 1600 \text{ km s}^{-1}$), spatially resolved, biconical molecular outflows in IRAS 20100–4156 and IRAS 03158+4227, and conservative mass outflow rates

of $\sim 300 - 700 M_{\odot} \text{ yr}^{-1}$. Based on their observed gas masses, we infer gas depletion timescales of $\tau_{\text{OF}}^{\text{dep}} \sim 11$ and $\tau_{\text{OF}}^{\text{dep}} \sim 16 \text{ Myr}$ respectively. These are around ~ 3 times shorter than the gas depletion timescales due to star-formation, and demonstrate that extreme molecular outflows can starve the gas supply in galaxies on short timescales.

- We use multiple diagnostics to determine the AGN-fraction f_{AGN} in the two target sources. Based on mid-IR decomposition, X-ray observations, and SED fitting, we do not find a significant AGN fraction for IRAS 20100–4156, and a modest one for IRAS 03158+4227.
- We use mid-IR decomposition for an expanded sample of all published ULIRGs with molecular outflows observed using CO(1–0), and test for correlations between them. We find that extreme molecular outflows can be hosted by AGN-dominated, starburst dominated, and composite galaxies i.e. $f_{\text{AGN}} \sim 0.2 - 0.9$, and that the outflow energy and momenta are equally well correlated with AGN and starburst luminosities. While the outflow in IRAS 03158+4227 is consistent with being AGN-driven, we suggest that nuclear star formation may play an important role in driving the molecular outflow in IRAS 20100–4156.

We also highlight some of the future observations that are necessary for understanding the impact of molecular outflows on their host galaxies, and for better characterizing the outflow mass and energetics. This includes observations of (1) spatially resolved CO(1–0) in the molecular gas for a larger sample of ULIRGs to accurately obtain the outflow geometry and radius, (2) optically thin gas tracers, to accurately trace the outflow gas mass, and therefore the momentum and energy flux (3) future continuous monitoring of OH megamaser emission, providing very exciting avenues for future research. Observations such as these are well within the reach of current radio/mm/sub-mm interferometers (NOEMA, ALMA, and the VLA), and will allow us to build a comprehensive picture of the role of outflows in galaxy evolution.

We thank the anonymous referee for their helpful comments which significantly improved the clarity of the manuscript. We are grateful to E. Nardini for helping us with the starburst and AGN templates for the mid-IR decomposition. We thank Prof. Lister Staveley-Smith for providing us with Parkes OH megamaser spectra for IRAS 20100–4156. We also thank H. Meusinger for

providing us with optical data for IRAS 03158+4227. A.G thanks Cody Lamarche for many fruitful discussions. D.R. acknowledges support from the National Science Foundation under grant number AST-1614213 to Cornell University. E.GA is a Research Associate at the Harvard-Smithsonian Center for Astrophysics, and thanks the Spanish Ministerio de Economía y Competitividad for support under project ESP2015-65597-C4-1-R, and thanks NASA grant ADAP NNX15AE56G. Basic research in IR astronomy at NRL is funded by the US-ONR; J.F. acknowledges support from NHSC/ JPL sub-contracts 139807 and 1456609. CF acknowledges support from the European Union Horizon 2020 research and innovation programme under the Marie Skłodowska-Curie grant agreement No. 664931. J.A. gratefully acknowledges support from the Science and Technology Foundation (FCT, Portugal) through the research grant PTDC/FIS-AST/2194/2012 and UID/FIS/04434/2013. This paper makes use of the following ALMA data: ADS/JAO.ALMA#2013.1.00659.S. ALMA is a partnership of ESO (representing its member states), NSF (USA) and NINS (Japan), together with NRC (Canada) and NSC and ASIAA (Taiwan) and KASI (Republic of Korea), in cooperation with the Republic of Chile. The Joint ALMA Observatory is operated by ESO, AUI/NRAO and NAOJ. The National Radio Astronomy Observatory is a facility of the National Science

Foundation operated under cooperative agreement by Associated Universities, Inc. Funding for the Sloan Digital Sky Survey IV has been provided by the Alfred P. Sloan Foundation, the U.S. Department of Energy Office of Science, and the Participating Institutions. SDSS-IV acknowledges support and resources from the Center for High-Performance Computing at the University of Utah. The SDSS web site is www.sdss.org. Based on observations carried out under project ID W08E with the IRAM NOEMA Interferometer. IRAM is supported by INSU/CNRS (France), MPG (Germany) and IGN (Spain). This publication is based on data acquired with the Atacama Pathfinder Experiment (APEX) under programme ID 090.B-0404. APEX is a collaboration between the Max-Planck-Institut für Radioastronomie, the European Southern Observatory, and the Onsala Space Observatory. This research has made use of the NASA/IPAC Extragalactic Database (NED) which is operated by the Jet Propulsion Laboratory, California Institute of Technology, under contract with the National Aeronautics and Space Administration.

Facilities: ALMA, EVLA, HST, APEX, IRAM, *Herschel*, *Spitzer*

Software: CASA (McMullin et al. 2007), GILDAS (Pety 2005), Astropy (Astropy Collaboration et al. 2013), CIGALE (Noll et al. 2009), DS9, GAIA Skycat

APPENDIX

Here we present the details of model-fitting to the visibilities for the red- and blue-shifted outflow wings in IRAS 20100–4156 and IRAS 03158+4227. The fits to the uv visibility data for the red and blue wings are described by six parameters: the integrated flux (I), offsets from the phase center (δx and δy), the FWHM along the major axis (a), the axial ratio between the semi-minor and semi-major axes (r), and the position angle (PA). Note that the phase-centers were shifted to the centroids of the red and blue-shifted emission from the moment-0 maps before the fitting, resulting in the small offsets found in the model. The best uv -model fits are shown in Fig. 17, and their parameters are listed in Table 6. We see evidence that a 2-D Gaussian does not fully reproduce the data for IRAS 20100–4156 on the longest baselines, indicating that the red and blue outflow wings are individually marginally resolved in our observations and that they deviate from elliptical Gaussians on the smallest scales (Fig. 17). For IRAS 03158+4227, the visibilities suffer from greater uncertainties on shorter baselines (i.e. larger spatial scales) due to a relatively sparse uv -coverage on those scales.

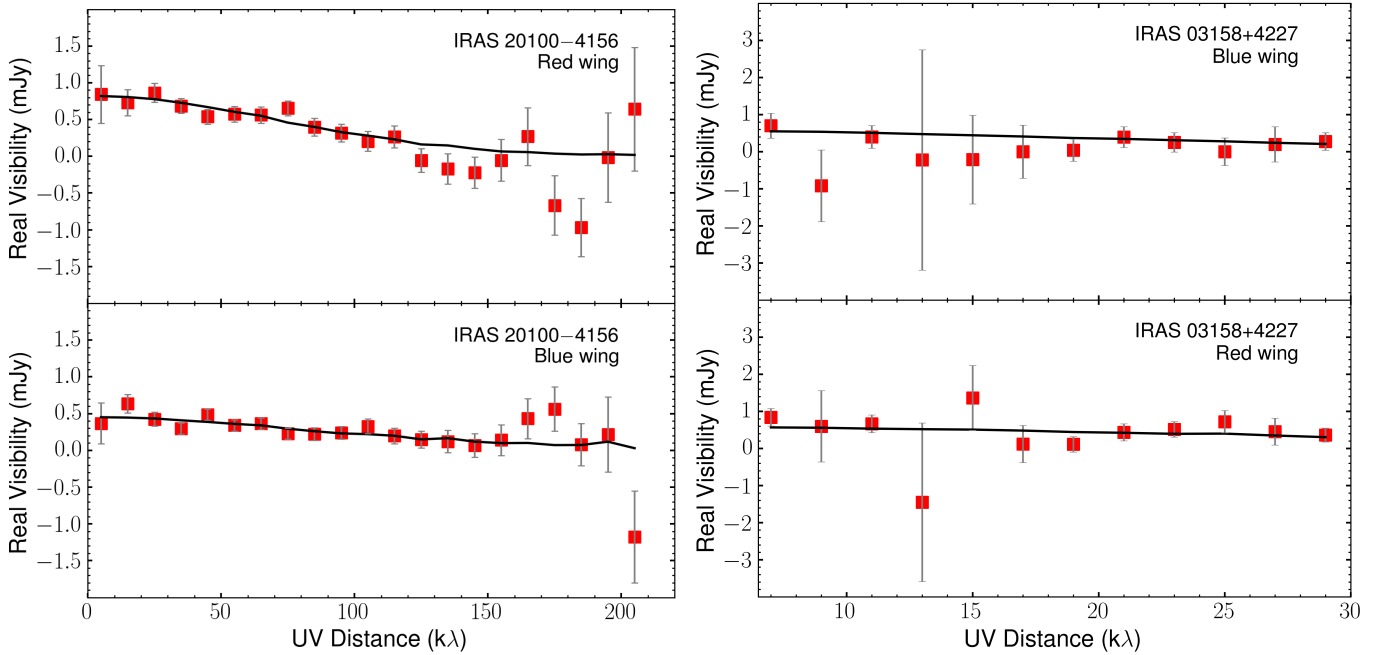
REFERENCES

- | | |
|--|--|
| <p>Aalto, S., Polatidis, A. G., Hüttemeister, S., & Curran, S. J. 2002, <i>A&A</i>, 381, 783</p> <p>Alatalo, K., Lacy, M., Lanz, L., et al. 2015, <i>ApJ</i>, 798, 31</p> <p>Alonso-Herrero, A. 2013, <i>ArXiv e-prints</i>, arXiv:1302.2033</p> <p>Alonso-Herrero, A., Pereira-Santaella, M., Rieke, G. H., & Rigopoulou, D. 2012, <i>ApJ</i>, 744, 2</p> <p>Astropy Collaboration, Robitaille, T. P., Tollerud, E. J., et al. 2013, <i>A&A</i>, 558, A33</p> | <p>Baan, W. A., Haschick, A. D., & Henkel, C. 1989, <i>ApJ</i>, 346, 680</p> <p>Baan, W. A., Rhoads, J., Fisher, K., Altschuler, D. R., & Haschick, A. 1992, <i>ApJL</i>, 396, L99</p> <p>Ballo, L., Braito, V., Della Ceca, R., et al. 2004, <i>ApJ</i>, 600, 634</p> <p>Balmaverde, B., Marconi, A., Brusa, M., et al. 2016, <i>A&A</i>, 585, A148</p> |
|--|--|

Table 6. Description of UVMODELFIT results for red and blue-shifted emission.

Parameter	IRAS 20100–4156		IRAS 03158+4227	
	Red wing	Blue wing	Red wing	Blue wing
RA ^a	20 ^h 13 ^m 29.577 ^s	20 ^h 13 ^m 29.536 ^s	03 ^h 19 ^m 11.896 ^s	03 ^h 19 ^m 12.003 ^s
Dec ^a	−41 ^d 47 ^m 35.550 ^s	−41 ^d 47 ^m 34.997 ^s	+42 ^d 38 ^m 25.374 ^s	+42 ^d 38 ^m 24.285 ^s
I (10 ^{−4} Jy)	4.3 ± 0.3	8.2 ± 0.4	5.9 ± 1.6	5.9 ± 2.8
δx (arcsec)	0.07 ± 0.03	−0.03 ± 0.03	0.1 ± 0.4	0.03 ± 0.8
δy (arcsec)	0.00 ± 0.03	0.05 ± 0.03	−0.01 ± 0.40	0.02 ± 0.80
a (arcsec)	0.8 ± 0.1	1.3 ± 0.1	3.3 ± 1.3	3.8 ± 2.6
r	1.0 ± 0.2	0.6 ± 0.1	0.8 ± 0.5	1.0 ± 0.9
PA (°)	74 ± 57	−28 ± 8	−31 ± 82	−52 ± 57

^aThe assumed phase centers for the red and blue-shifted emission, obtained from the centroid of the moment-0 maps for each.

**Figure 17.** Results of using UVMODELFIT to model the visibilities for each of the red and blue outflow wings in IRAS 03158+4227 and IRAS 20100–4156, assuming that the outflow emission can be represented by a 2D Gaussian.

Baugh, C. M., Cole, S., Frenk, C. S., & Lacey, C. G. 1998, *ApJ*, 498, 504

Benson, A. J., Bower, R. G., Frenk, C. S., et al. 2003, *ApJ*, 599, 38

Blanton, M. R., Bershad, M. A., Abolfathi, B., et al. 2017, *AJ*, 154, 28

Bolatto, A. D., Wolfire, M., & Leroy, A. K. 2013, *ARA&A*, 51, 207

Bower, R. G., Benson, A. J., Malbon, R., et al. 2006, *MNRAS*, 370, 645

Brandl, B. R., Bernard-Salas, J., Spoon, H. W. W., et al. 2006, *ApJ*, 653, 1129

Bruzual, G., & Charlot, S. 2003, *MNRAS*, 344, 1000

Bushouse, H. A., Borne, K. D., Colina, L., et al. 2002, *ApJS*, 138, 1

Calzetti, D., Armus, L., Bohlin, R. C., et al. 2000, *ApJ*, 533, 682

Capak, P. L., Teplitz, H. I., Brooke, T. Y., Laher, R., & Science Center, S. 2013, in *American Astronomical Society Meeting Abstracts*, Vol. 221, American Astronomical Society Meeting Abstracts #221, 340.06

Casey, C. M. 2012, *MNRAS*, 425, 3094

Casey, C. M., Narayanan, D., & Cooray, A. 2014, *PhR*, 541, 45

- Cen, R. 2012, *ApJ*, 755, 28
- Cicone, C., Feruglio, C., Maiolino, R., et al. 2012, *A&A*, 543, A99
- Cicone, C., Maiolino, R., Sturm, E., et al. 2014, *A&A*, 562, A21
- Cui, J., Xia, X.-Y., Deng, Z.-G., Mao, S., & Zou, Z.-L. 2001, *AJ*, 122, 63
- Dale, D. A., Helou, G., Magdis, G. E., et al. 2014, *ApJ*, 784, 83
- Darling, J. 2007, *ApJL*, 669, L9
- Darling, J., & Giovanelli, R. 2002a, *ApJ*, 572, 810
- . 2002b, *AJ*, 124, 100
- Davis, S. W., Jiang, Y.-F., Stone, J. M., & Murray, N. 2014, *ApJ*, 796, 107
- Draine, B. T., & Li, A. 2007, *ApJ*, 657, 810
- Draine, B. T., Aniano, G., Krause, O., et al. 2014, *ApJ*, 780, 172
- Efstathiou, A., Pearson, C., Farrah, D., et al. 2014, *MNRAS*, 437, L16
- Elvis, M., Wilkes, B. J., McDowell, J. C., et al. 1994, *ApJS*, 95, 1
- Farrah, D., Afonso, J., Efstathiou, A., et al. 2003, *MNRAS*, 343, 585
- Farrah, D., Serjeant, S., Efstathiou, A., Rowan-Robinson, M., & Verma, A. 2002, *MNRAS*, 335, 1163
- Farrah, D., Bernard-Salas, J., Spoon, H. W. W., et al. 2007, *ApJ*, 667, 149
- Farrah, D., Urrutia, T., Lacy, M., et al. 2012, *ApJ*, 745, 178
- Farrah, D., Leboutteiller, V., Spoon, H. W. W., et al. 2013, *ApJ*, 776, 38
- Faucher-Giguère, C.-A., & Quataert, E. 2012, *MNRAS*, 425, 605
- Ferrarese, L., & Merritt, D. 2000, *ApJL*, 539, L9
- Feruglio, C., Maiolino, R., Piconcelli, E., et al. 2010, *A&A*, 518, L155
- Feruglio, C., Fiore, F., Carniani, S., et al. 2015, *A&A*, 583, A99
- Fischer, J., Sturm, E., González-Alfonso, E., et al. 2010, *A&A*, 518, L41
- Franceschini, A., Braito, V., Persic, M., et al. 2003, *MNRAS*, 343, 1181
- Fritz, J., Franceschini, A., & Hatziminaoglou, E. 2006, *MNRAS*, 366, 767
- Gao, Y., & Solomon, P. M. 2004a, *ApJS*, 152, 63
- . 2004b, *ApJ*, 606, 271
- García-Burillo, S., Combes, F., Usero, A., et al. 2015, *A&A*, 580, A35
- Geach, J. E., Hickox, R. C., Diamond-Stanic, A. M., et al. 2014, *Nature*, 516, 68
- Gebhardt, K., Bender, R., Bower, G., et al. 2000, *ApJL*, 539, L13
- Genzel, R., Lutz, D., Sturm, E., et al. 1998, *ApJ*, 498, 579
- González-Alfonso, E., Fischer, J., Sturm, E., et al. 2015, *ApJ*, 800, 69
- González-Alfonso, E., Fischer, J., Spoon, H. W. W., et al. 2017, *ApJ*, 836, 11
- González-Alfonso, E., Fischer, J., Bruderer, S., et al. 2018, *ArXiv e-prints*, arXiv:1803.04690
- Harvey-Smith, L., Allison, J. R., Green, J. A., et al. 2016, *MNRAS*, 460, 2180
- Heckman, T. M., Alexandroff, R. M., Borthakur, S., Overzier, R., & Leitherer, C. 2015, *ApJ*, 809, 147
- Heckman, T. M., & Borthakur, S. 2016, *ApJ*, 822, 9
- Hopkins, P. F. 2012, *MNRAS*, 420, L8
- Houck, J. R., Roellig, T. L., van Cleve, J., et al. 2004, *ApJS*, 154, 18
- Inami, H., Armus, L., Charmandaris, V., et al. 2013, *ApJ*, 777, 156
- Ishibashi, W., Auger, M. W., Zhang, D., & Fabian, A. C. 2014, *MNRAS*, 443, 1339
- Ishibashi, W., Fabian, A. C., & Canning, R. E. A. 2013, *MNRAS*, 431, 2350
- Jahnke, K., & Macciò, A. V. 2011, *ApJ*, 734, 92
- Kewley, L. J., Groves, B., Kauffmann, G., & Heckman, T. 2006, *MNRAS*, 372, 961
- King, A., & Pounds, K. 2015, *ARA&A*, 53, 115
- King, A. R. 2010, *MNRAS*, 402, 1516
- Klöckner, H.-R., Baan, W. A., & Garrett, M. A. 2003, *Nature*, 421, 821
- Krumholz, M. R., & Thompson, T. A. 2013, *MNRAS*, 434, 2329
- Lapi, A., Cavaliere, A., & Menci, N. 2005, *ApJ*, 619, 60
- Laurent, O., Mirabel, I. F., Charmandaris, V., et al. 2000, *A&A*, 359, 887
- Leboutteiller, V., Barry, D. J., Goes, C., et al. 2015, *ApJS*, 218, 21
- Leboutteiller, V., Barry, D. J., Spoon, H. W. W., et al. 2011, *ApJS*, 196, 8
- Leitherer, C., Schaerer, D., Goldader, J. D., et al. 1999, *ApJS*, 123, 3
- Lo, K. Y. 2005, *ARA&A*, 43, 625
- Lonsdale, C. J., Diamond, P. J., Lonsdale, C. J., & Smith, H. E. 1998, in *Astronomical Society of the Pacific Conference Series*, Vol. 144, IAU Colloq. 164: Radio Emission from Galactic and Extragalactic Compact Sources, ed. J. A. Zensus, G. B. Taylor, & J. M. Wrobel, 227
- Lonsdale, C. J., Lonsdale, C. J., Smith, H. E., & Diamond, P. J. 2003, *ApJ*, 592, 804

- Lusso, E., Comastri, A., Vignali, C., et al. 2010, *A&A*, 512, A34
- Lusso, E., Comastri, A., Simmons, B. D., et al. 2012, *MNRAS*, 425, 623
- Magorrian, J., Tremaine, S., Richstone, D., et al. 1998, *AJ*, 115, 2285
- Maiolino, R., Gallerani, S., Neri, R., et al. 2012, *MNRAS*, 425, L66
- Maiolino, R., Russell, H. R., Fabian, A. C., et al. 2017, *Nature*, 544, 202
- Maraston, C. 2005, *MNRAS*, 362, 799
- Marconi, A., Risaliti, G., Gilli, R., et al. 2004, *MNRAS*, 351, 169
- McConnell, N. J., & Ma, C.-P. 2013, *ApJ*, 764, 184
- McMullin, J. P., Waters, B., Schiebel, D., Young, W., & Golap, K. 2007, in *Astronomical Society of the Pacific Conference Series*, Vol. 376, *Astronomical Data Analysis Software and Systems XVI*, ed. R. A. Shaw, F. Hill, & D. J. Bell, 127
- Meusinger, H., Stecklum, B., Theis, C., & Brunzendorf, J. 2001, *A&A*, 379, 845
- Murray, N., Quataert, E., & Thompson, T. A. 2005, *ApJ*, 618, 569
- Nardini, E., & Risaliti, G. 2011, *MNRAS*, 415, 619
- Nardini, E., Risaliti, G., Salvati, M., et al. 2008, *MNRAS*, 385, L130
- . 2009, *MNRAS*, 399, 1373
- Nardini, E., Risaliti, G., Watabe, Y., Salvati, M., & Sani, E. 2010, *MNRAS*, 405, 2505
- Nardini, E., Reeves, J. N., Gofford, J., et al. 2015, *Science*, 347, 860
- Noll, S., Burgarella, D., Giovannoli, E., et al. 2009, *A&A*, 507, 1793
- Novak, G. S., Ostriker, J. P., & Ciotti, L. 2012, *MNRAS*, 427, 2734
- Oosterloo, T., Oonk, J. B. R., Morganti, R., et al. 2017, *ArXiv e-prints*, arXiv:1710.01570
- Papadopoulos, P. P., van der Werf, P., Isaak, K., & Xilouris, E. M. 2010, *ApJ*, 715, 775
- Papadopoulos, P. P., van der Werf, P., Xilouris, E., Isaak, K. G., & Gao, Y. 2012, *ApJ*, 751, 10
- Pearson, C., Rigopoulou, D., Hurley, P., et al. 2016a, *ApJS*, 227, 9
- . 2016b, *ApJS*, 227, 9
- Pérez-Beaupuits, J. P., Aalto, S., & Gerebro, H. 2007, *A&A*, 476, 177
- Pety, J. 2005, in *SF2A-2005: Semaine de l’Astrophysique Française*, ed. F. Casoli, T. Contini, J. M. Hameury, & L. Pagani, 721
- Pihlström, Y. M., Baan, W. A., Darling, J., & Klöckner, H.-R. 2005, *ApJ*, 618, 705
- Pihlström, Y. M., Conway, J. E., Booth, R. S., Diamond, P. J., & Polatidis, A. G. 2001, *A&A*, 377, 413
- Pitchford, L. K., Hatziminaoglou, E., Feltre, A., et al. 2016, *MNRAS*, 462, 4067
- Ranalli, P., Comastri, A., & Setti, G. 2003, *A&A*, 399, 39
- Rémy-Ruyer, A., Madden, S. C., Galliano, F., et al. 2014, *A&A*, 563, A31
- Richings, A. J., & Faucher-Giguere, C.-A. 2017a, *ArXiv e-prints*, arXiv:1706.03784
- . 2017b, *ArXiv e-prints*, arXiv:1710.09433
- Risaliti, G., Gilli, R., Maiolino, R., & Salvati, M. 2000, *A&A*, 357, 13
- Rodriguez-Franco, A., Martin-Pintado, J., & Fuente, A. 1998, *A&A*, 329, 1097
- Rosenberg, M. J. F., van der Werf, P. P., Aalto, S., et al. 2015, *ApJ*, 801, 72
- Roth, N., Kasen, D., Hopkins, P. F., & Quataert, E. 2012, *ApJ*, 759, 36
- Rovilos, E., Diamond, P. J., Lonsdale, C. J., Lonsdale, C. J., & Smith, H. E. 2003, *MNRAS*, 342, 373
- Rupke, D. S., Veilleux, S., & Sanders, D. B. 2005, *ApJS*, 160, 115
- Sakamoto, K., Wang, J., Wiedner, M. C., et al. 2008, *ApJ*, 684, 957
- Sanders, D. B., & Mirabel, I. F. 1996, *ARA&A*, 34, 749
- SDSS Collaboration, Albareti, F. D., Allende Prieto, C., et al. 2016, *ArXiv e-prints*, arXiv:1608.02013
- Serra, P., Amblard, A., Temi, P., et al. 2011, *ApJ*, 740, 22
- Silk, J., & Nusser, A. 2010, *ApJ*, 725, 556
- Skinner, M. A., & Ostriker, E. C. 2015, *ApJ*, 809, 187
- Skrutskie, M. F., Cutri, R. M., Stiening, R., et al. 2006, *AJ*, 131, 1163
- Somerville, R. S., Hopkins, P. F., Cox, T. J., Robertson, B. E., & Hernquist, L. 2008, *MNRAS*, 391, 481
- Spergel, D. N., Bean, R., Doré, O., et al. 2007, *ApJS*, 170, 377
- Spoon, H. W. W., & Holt, J. 2009, *ApJL*, 702, L42
- Spoon, H. W. W., Marshall, J. A., Houck, J. R., et al. 2007, *ApJL*, 654, L49
- Spoon, H. W. W., Armus, L., Cami, J., et al. 2004, *ApJS*, 154, 184
- Spoon, H. W. W., Farrah, D., Leboutteiller, V., et al. 2013, *ApJ*, 775, 127
- Staveley-Smith, L., Allen, D. A., Chapman, J. M., Norris, R. P., & Whiteoak, J. B. 1989, *Nature*, 337, 625
- Staveley-Smith, L., Norris, R. P., Chapman, J. M., et al. 1992, *MNRAS*, 258, 725

- Stone, M., Veilleux, S., Meléndez, M., et al. 2016, *ApJ*, 826, 111
- Sturm, E., González-Alfonso, E., Veilleux, S., et al. 2011, *ApJL*, 733, L16
- Teng, S. H., Brandt, W. N., Harrison, F. A., et al. 2014, *ApJ*, 785, 19
- Teng, S. H., Rigby, J. R., Stern, D., et al. 2015, *ApJ*, 814, 56
- Thompson, T. A., Fabian, A. C., Quataert, E., & Murray, N. 2015, *MNRAS*, 449, 147
- Thompson, T. A., Quataert, E., & Murray, N. 2005, *ApJ*, 630, 167
- Tombesi, F., Meléndez, M., Veilleux, S., et al. 2015, *Nature*, 519, 436
- Tsang, B. T.-H., & Milosavljević, M. 2015, *MNRAS*, 453, 1108
- Vasudevan, R. V., & Fabian, A. C. 2009, *MNRAS*, 392, 1124
- Veilleux, S., Bolatto, A., Tombesi, F., et al. 2017, *ApJ*, 843, 18
- Veilleux, S., Cecil, G., & Bland-Hawthorn, J. 2005, *ARA&A*, 43, 769
- Veilleux, S., Rupke, D. S. N., Kim, D.-C., et al. 2009, *ApJS*, 182, 628
- Veilleux, S., Meléndez, M., Sturm, E., et al. 2013, *ApJ*, 776, 27
- Violino, G., Coppin, K. E. K., Stevens, J. A., et al. 2016, *MNRAS*, 457, 1371
- Weaver, R., McCray, R., Castor, J., Shapiro, P., & Moore, R. 1977, *ApJ*, 218, 377
- Willett, K. W., Darling, J., Spoon, H. W. W., Charmandaris, V., & Armus, L. 2011, *ApJS*, 193, 18
- Wilson, C. D., Petitpas, G. R., Iono, D., et al. 2008, *ApJS*, 178, 189
- Xu, L., Rieke, G. H., Egami, E., et al. 2015, *ApJ*, 808, 159
- Yu, Z.-y. 2003, *MNRAS*, 338, 745
- Zubovas, K., & King, A. R. 2012, *MNRAS*, 426, 2751